Eur. Phys. J. A **26**, 399–419 (2005)
DOI 10.1140/epja/i2005-10191-2

THE EUROPEAN PHYSICAL JOURNAL A

Measurement of π^0 photoproduction on the proton from 550 to 1500 MeV at GRAAL

O. Bartalini[2,9], V. Bellini[1,5], J.P. Bocquet[12], M. Capogni[2,9,a], L. Casano[9], M. Castoldi[7], P. Calvat[12], A. D'Angelo[2,9], R. Di Salvo[9], A. Fantini[2,9], C. Gaulard[4,b], G. Gervino[3,10], F. Ghio[8,11], B. Girolami[8,11], A. Giusa[1,6], V. Kouznetsov[13], A. Lapik[13], P. Levi Sandri[4], A. Lleres[12,c], D. Moricciani[9], A.N. Mushkarenkov[13], V. Nedorezov[13], L. Nicoletti[2,9,12], C. Perrin[12], D. Rebreyend[12], F. Renard[12], N. Rudnev[13], T. Russew[12], G. Russo[1,6], C. Schaerf[2,9], M.-L. Sperduto[1,6], M.-C. Sutera[6], and A. Turinge[13]

[1] Dipartimento di Fisica ed Astronomia, Università di Catania, via Santa Sofia 64, I-95123 Catania, Italy
[2] Dipartimento di Fisica, Università di Roma "Tor Vergata", via della Ricerca Scientifica 1, I-00133 Roma, Italy
[3] Dipartimento di Fisica Sperimentale, Università di Torino, via P. Giuria, I-00125 Torino, Italy
[4] INFN - Laboratori Nazionali di Frascati, via E. Fermi 40, I-00044 Frascati (Roma), Italy
[5] INFN - Laboratori Nazionali del Sud, via Santa Sofia 44, I-95123 Catania, Italy
[6] INFN - Sezione di Catania, via Santa Sofia 64, I-95123 Catania, Italy
[7] INFN - Sezione di Genova, via Dodecanneso 33, I-16146 Genova, Italy
[8] INFN - Sezione di Roma I, piazzale Aldo Moro 2, I-00185 Roma, Italy
[9] INFN - Sezione di Roma II, via della Ricerca Scientifica 1, I-00133 Roma, Italy
[10] INFN - Sezione di Torino, I-10125 Torino, Italy
[11] Instituto Superiore di Sanità, viale Regina Elena 299, I-00161 Roma, Italy
[12] IN2P3, Laboratoire de Physique Subatomique et de Cosmologie, F-38026 Grenoble, France
[13] Institute for Nuclear Research, 117312 Moscow, Russia

Received: 27 June 2005 / Revised version: 3 November 2005 /
Published online: 23 January 2006 –
Communicated by P. Picozza

Abstract. Neutral pion photoproduction has been measured from 550 to 1500 MeV with the GRAAL facility, located at the ESRF in Grenoble. Differential cross-section and beam asymmetry have been measured over a wide angular range. These high-precision data improve significantly the database for the beam asymmetry in the second and third resonance regions covering for the first time the energy domain 1100–1500 MeV. New partial-wave analyses including these data are presented for which the beam asymmetry brings crucial constraints.

PACS. 13.60.Le Meson production – 13.88.+e Polarization in interactions and scattering – 25.20.Lj Photoproduction reactions

1 Introduction

Thanks to the recent development of new accelerators worldwide, meson photoproduction (or more generally electroproduction) is nowadays a major tool to investigate N^* properties [1]. Due to its simplicity and high production rate, single-pion photoproduction plays a special role and has already been abundantly studied. Most of the N^* electromagnetic couplings have been extracted through multipole analyses of these channels [2].

Until recently, the database was containing essentially cross-section results often with poor statistics and limited angular range. With the onset of new facilities (Bonn-ELSA, GRAAL, JLab-CLAS, LEGS, LEPS and Mainz-MAMI), using systematically polarized beam and/or target combined with large-acceptance detectors, the experimental context has now significantly improved. In particular, the beam asymmetry Σ, accessible with a linearly polarized beam, has proven recently to be particularly sensitive to the resonant contributions. For instance, in the region of the Δ-resonance, a major effort has been undertaken over the last decade to extract the tiny $E2/M1$ ratio in the N-Δ transition for which high-precision data have been obtained [3,4]. Thanks to the beam asymmetry, an impressive accuracy has now been achieved on this ratio,

[a] *Present address*: ENEA - C.R. Casaccia, via Anguillarese 301, I-00060 Roma, Italy.
[b] *Present address*: IN2P3, Centre de Spectrométrie Nucléaire et de Spectrométrie de Masse, F-91405 Orsay, France.
[c] e-mail: `lleres@lpsc.in2p3.fr`

despite some model dependence in the extraction, and its value differs largely from older results. On the other hand, we have recently measured Σ over a large angular range for the reactions $\gamma p \to \pi^+ n$, $\gamma p \to \eta p$ and $\gamma p \to \pi^0\pi^0 p$ in the second and third resonance regions [5–8]. For all these channels, Σ provided severe constraints on the reaction mechanism. In particular, Σ has been the key for the quantitative determination of the $D_{13}(1520)$ contribution in η photoproduction [9–12].

In the present work, we report on measurements of the beam asymmetry Σ and of the differential cross-section for the reaction $\gamma p \to \pi^0 p$ over large energy ($E_\gamma = 550$–1500 MeV, $W = 1400$–1900 MeV) and angular ($\theta^{\rm CM} = 40$–$170°$) ranges. For the first time, the region above 1100 MeV is extensively covered with high-precision Σ data.

2 The GRAAL set-up

2.1 General layout

This experiment has been carried-out with the GRAAL facility (fig. 1), installed at the European Synchrotron Radiation Facility (ESRF) in Grenoble (France). The tagged and polarized γ-ray beam is produced by Compton scattering of laser photons off the 6.03 GeV electrons circulating in the storage ring (844 m circumference), over a 6.5 m long straight section (so-called interaction region in fig. 1). Backscattered photons of useful energies are emitted in a narrow cone and impinge on a liquid-hydrogen target placed at 41.5 m from the center of the interaction region while the scattered electrons are detected in an internal tagging system. The beam size at the target is $\approx 2 \times 1$ cm^2. A primary collimator followed by a sweeping magnet is used only to cut the low-energy tails of the beam. Two secondary collimators placed under vacuum eliminate the multitude of low-energy photons produced by showers in the main collimator and are essential to get a reduced electromagnetic background in the detector. Before reaching a SPACAL-type calorimeter (scintillating fibers embedded in a lead matrix) [13] which serves also as beam dump, photons pass through a thin monitor used to measure the beam flux.

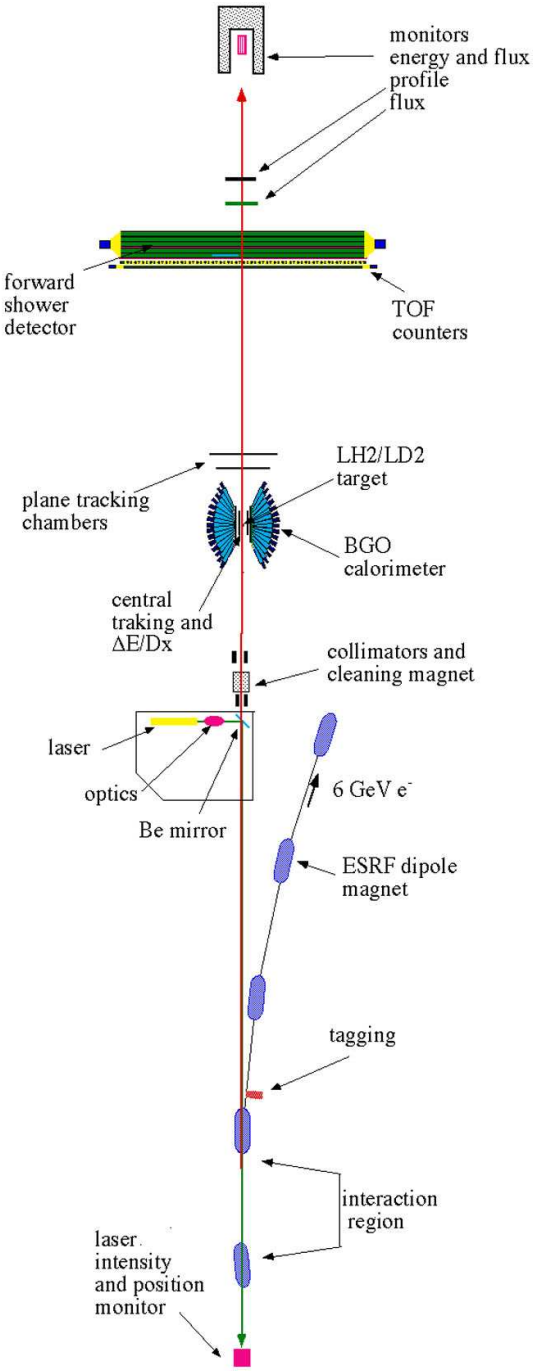

Fig. 1. General layout of the GRAAL set-up (the drawing is out of scale).

2.2 Compton beam

In the case of Compton scattering of low-energy photons off ultra-relativistic electrons, the energy dependence of the scattered photon *versus* angle in the laboratory frame reduces to

$$E_\gamma = \frac{4\gamma^2 E_L}{1 + \frac{4\gamma E_L}{m_e} + \theta^2\gamma^2}\,, \qquad (1)$$

where θ is the angle between the scattered photon and the incident direction of the electron, γ is the Lorentz factor of the electron (≈ 12000 for the 6 GeV ESRF beam), E_L the energy of the incident photon and m_e the mass of the

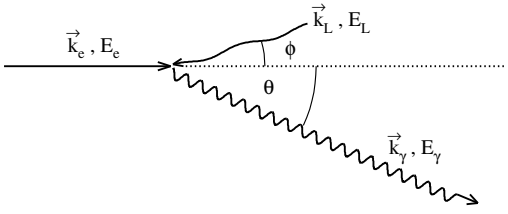

Fig. 2. Definition of Compton-scattering kinematical variables.

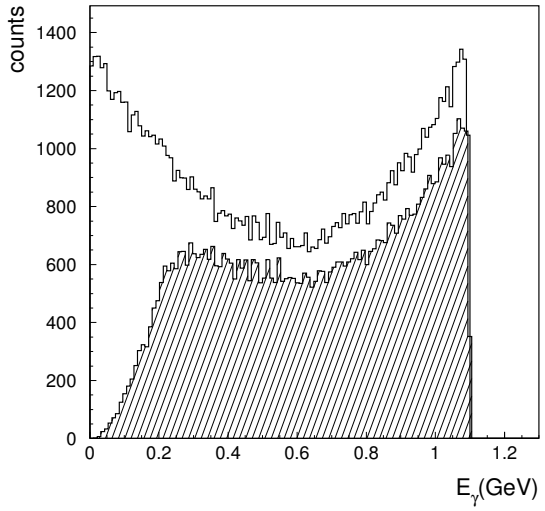

Fig. 3. Simulated Compton energy spectrum for $\lambda = 514$ nm. The initial spectrum is compared to the spectrum at the target (hatched histogram). The low-energy cut is due to collimation while the difference at medium and high energy is due to the various elements on the path of the γ-ray beam (windows, Be mirror, ...).

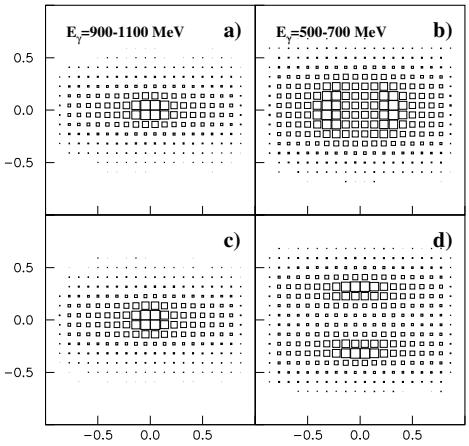

Fig. 4. Simulated transverse beam profile at the target ($\lambda = 514$ nm) for two photon energy ranges and for the two linear polarization states: vertical (a, b) and horizontal (c, d). The scales are in cm.

electron (fig. 2). The ϕ angle between the incoming photon and the electron beam axis cannot exceed 1° given the geometry of the set-up and has no measurable influence. The maximum photon energy (Compton edge) depends on the laser wavelength. For the present experiment, we have used alternately the green line at 514 nm and a set of UV lines (MLUV) at 333, 351 and 364 nm produced by an Ar laser, giving 1.1, 1.4, 1.47 and 1.53 GeV Compton edges, respectively. By contrast to Bremsstrahlung beam, the energy spectrum is rather flat and the low-energy photons can be suppressed by collimation before they reach the target (fig. 3).

As illustrated in fig. 4, Compton scattering generates a beam shape strongly energy and polarization dependent.

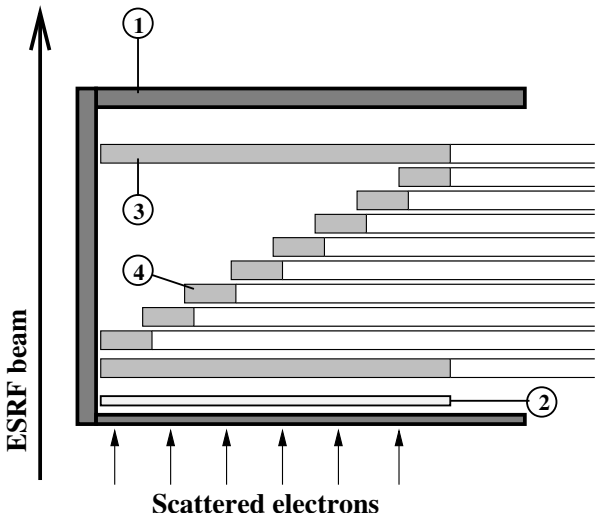

Fig. 5. Schematic drawing of the tagging detector: 1) X-ray shielding, 2) Si microstrip detector, 3), 4) Scintillators and light guides. See text for more details

2.2.1 Simulation

The γ-ray beam properties (resolution, polarization, intensity) depend critically on numerous optical and geometrical parameters. In order to assess their effect and optimize the beam characteristics, we have developed a complete simulation with the GEANT3 code from the CERN library. It includes a realistic description of the beam line from the interaction region to the beam dump, of the tagging system for the scattered electrons and takes precisely into account the electron beam optics and the shape of the laser beam.

2.2.2 Photon energy and tagging system

The photon energy is provided by an internal tagging system (fig. 5) located right after the exit dipole of the interaction region (fig. 1). The position of the scattered electron is measured by a silicon microstrip detector (128 strips with a pitch of 300 μm and 1000 μm thick). Two long plastic scintillators covering most of the focal plane (38.4 mm) and eight additional small ones (6.8 mm long) are situated behind the microstrip detector. The small scintillators overlap each of the neighbouring ones by 2 mm along the direction of the incoming electron beam. The signal rise time of the plastic scintillators is less than 1.8 ns and a custom made electronics, based on GaAs technology, provides the synchronization of the discriminated signal of one of the long scintillators with the RF signal of the electron beam. The final logical signal has a total time jitter less than 100 ps with respect to the timing of the electron beam and is capable of separating two electrons of adjacent bunches (2.8 ns). This signal drives a triple coincidence (called "TAG" hereafter) with the second long scintillator and any of the small plastic scintillators that provides an excellent global start signal for all Time-of-Flight

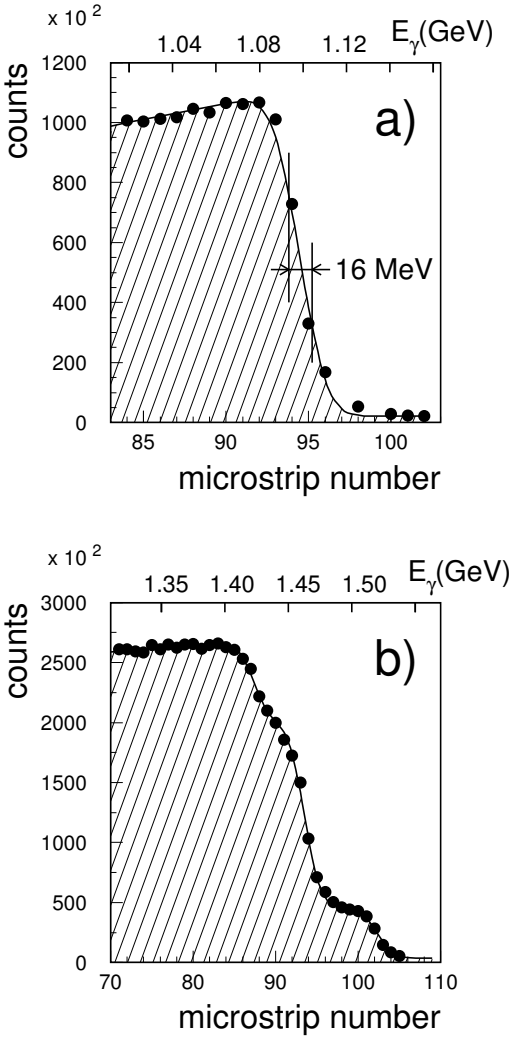

Fig. 6. Compton edges measured by the tagging system for two different laser settings: a) green line (514 nm) and b) Multi-Line UV (364, 351, 333 nm). The three lines are clearly resolved. The solid lines represent the fitted curves from which the energy resolution (16 MeV FWHM) and the Compton-edge position (with an accuracy of 0.03 μstrip) are extracted. See text for more details.

(ToF) measurements and enters in the different triggers (see sect. 2.5) of the experiment.

The whole system is shielded against the huge X-ray background by a 4π box made of stainless steel and tungsten and having a total thickness equivalent to 8 mm of lead. The thickness of this box and the minimum distance allowed between its wall and the electron beam determines our threshold of 550 MeV. The high-energy part of the Compton spectrum measured by the microstrip detector is displayed in fig. 6 for the green and MLUV settings of the laser. As illustrated in this figure, the experimental energy resolution can be directly extracted from the fit of the Compton edge with an error function. The measured resolution of 16 MeV (FWHM) is in agreement with the estimated one from the simulation and is dominated by the energy spread of the electrons in the storage ring (FWHM = 14 MeV). In the case of MLUV, the three edges are clearly resolved and their peak position and relative intensity can be extracted. The peak position of a given line is measured with a high accuracy (9 μm equivalent to 0.3 MeV).

The relation between the γ-ray energy E_γ and the distance, x_e, of the scattered electron to the beam axis can be approximated by the following expression:

$$E_\gamma = E_e \frac{x_e}{a_0 + x_e}\,, \tag{2}$$

where E_e is the electron beam energy and a_0 is a geometrical factor, constant to an excellent approximation over the tagged energy range ($da_0/a_0 = 5\ 10^{-4}$).

The beam energy given by the ESRF machine group, based on a $\int B\mathrm{d}l$ measurement over the ring, was:

$$E_e^{\mathrm{ESRF}} = 6040 \pm 20\ \mathrm{MeV}\,.$$

We have performed two independent measurements of this energy. First, by using the precisely known energy threshold of the reaction $\gamma p \to \eta p$, we have obtained a consistent value with an improved accuracy [14]:

$$E_e^{\eta} = 6030.6 \pm 6.0\ \mathrm{MeV}\,.$$

More recently, taking advantage of our ability to measure the transverse polarization of the stored electrons (Sokolov-Ternov effect), using the beam profiler of the GRAAL set-up, we have achieved an excellent precision on the beam energy by means of the resonant depolarization method [15]:

$$E_e^{\mathrm{RD}} = 6027.6 \pm 1.3\ \mathrm{MeV}\,.$$

The geometrical factor a_0 depends on the radius of curvature in the dipole and on the longitudinal position of the microstrip detector. Its value can be inferred from the distance between Compton edges associated with different laser lines. We have obtained:

$$a_0 = 159.92 \pm 0.3\ \mathrm{mm}\,,$$

Finally, the distance x_e of the scattered electron to the beam axis is

$$x_e = (n_{\mu\mathrm{strip}} - 0.5)\Delta x + x_0\,, \tag{3}$$

where $n_{\mu strip}$ is the number of the hit microstrip, Δx the pitch (300 μm) and x_0 the distance of the first microstrip to the stored electron beam. This latter parameter is deduced from the fit of the position of the Compton edge run by run.

Taking into account all possible sources of uncertainties, we estimate that the absolute error on the photon energy calibration does not exceed ≈ 2 MeV over the whole tagged range.

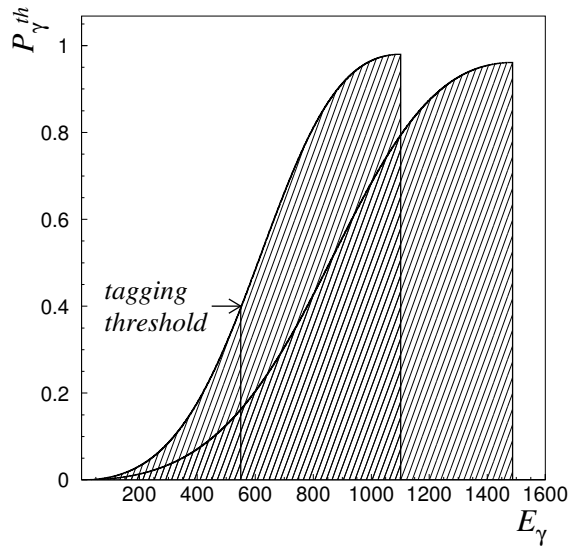

Fig. 7. Theoretical linear polarization of the γ-ray beam for two laser lines: $\lambda = 514$ nm (green line) and $\lambda = 351$ nm (UV line). The energy threshold (550 MeV) introduced by the tagging system is shown.

2.2.3 Beam polarization

The γ-ray beam polarization is calculated with the help of the Klein-Nishina formula and was first derived for such asymmetric collisions by Arutyunian *et al.* [16]. Its energy dependence is displayed in fig. 7 for two of the used wavelengths (514 nm, 351 nm) and in the case of a 100% linearly polarized laser beam. The γ-ray polarization is close to 1 at the Compton edge (98% for green and 96% for UV) and decreases smoothly with energy down to a minimum of $\approx 20\%$ at our energy threshold ($E_\gamma \approx 550$ MeV).

Below 1100 MeV, an asymmetry measurement can be performed with any of the two laser lines. This possibility has been used to perform an experimental cross-check of the polarization energy dependence presented in sect. 3.5.3.

Polarization of backscattered photons is proportional to the incident laser light polarization. Before each period of data taking, the laser polarization was measured into the laser hutch, after all optical elements. In order to avoid any distortion during the beam transport, a special viewport was used to minimize mechanical stress on the window. More recently, a new polarimeter has been installed after the intersection region into the ESRF tunnel and has allowed to confirm the previous measurements. We used a conservative value for the laser polarization and its associated error:

$$P_{\rm L} = 98 \pm 2\% \,.$$

Polarization calculation at one given energy —or equivalently at one given scattering angle θ— results from an integration over the azimuthal angle of all photons emitted at the same θ:

$$P(\theta) = \frac{\int P(\theta,\varphi)\frac{{\rm d}\sigma}{{\rm d}\Omega}(\theta,\varphi){\rm d}\varphi}{\int \frac{{\rm d}\sigma}{{\rm d}\Omega}(\theta,\varphi){\rm d}\varphi} \,. \quad (4)$$

With the help of the simulation, we have determined that a broad collimation (15×12 mm^2) was compatible with the target diameter (4 cm) while preserving the polarization of the low-energy tagged photons, even in the case of small drifts of the beam position.

Due to the scattering of electrons on the residual vacuum over the 6.5 m long interaction region, unpolarized Bremsstrahlung photons contaminate the Compton beam and affect the average degree of polarization. During the experiment, short periods of data acquisition were taken without laser (typically 5 min every 50 min) in order to measure the Bremsstrahlung background alone. Thanks to an excellent vacuum in the ring, the fraction of Bremsstrahlung photons $F_{\rm Brems}/F_{\rm Compton}$ remained of the order of 0.1% over the entire experiment.

In summary, we have used the following expression to calculate the beam polarization and its associated error:

$$P_\gamma = P_{\rm L} P_\gamma^{\rm th}\left(1 - \frac{F_{\rm Brems}}{F_{\rm Compton} + F_{\rm Brems}}\right), \quad (5)$$

$$\frac{\delta P_\gamma}{P_\gamma} = \sqrt{\left(\frac{\delta P_{\rm L}}{P_{\rm L}}\right)^2 + \left(\frac{\delta P_\gamma^{\rm th}}{P_\gamma^{\rm th}}\right)^2 + \left(\frac{\delta F_{\rm Brems}}{F_{\rm Compton} + F_{\rm Brems}}\right)^2}, \quad (6)$$

where $P_\gamma^{\rm th}$ is the calculated polarization. In the MLUV case, we took into account the superposition of the three laser lines with the measured relative intensities as described previously.

In practice, the only significant source of error came from the laser beam polarization:

$$\frac{\delta P_\gamma}{P_\gamma} = \frac{\delta P_{\rm L}}{P_{\rm L}} = 0.02 \,. \quad (7)$$

2.2.4 Flux monitoring

To avoid pile-up problems at high counting rate, the γ-ray beam intensity has been measured by means of a thin monitor. It consists of three plastic scintillators ($5\times5\times0.5$ cm^3), the first one acting as a veto, the two others being in coincidence, and a thin Al converter (2 mm) placed after the veto. Its efficiency ($2.68\%\pm0.03$) has been measured by comparison with the SPACAL absorber at low rate. It takes into account the γ-ray conversion between the target and the thin monitor and it is found experimentally independent of the γ-ray energy in the covered range. The typical flux during the experiment was 10^6 Hz.

2.3 The LH2 target

The target cell is an aluminum hollow cylinder of 4 cm in diameter closed by thin mylar windows (100 μm) at both ends. To satisfy different experimental requirements (resolution *versus* counting rates), three different lengths (3,

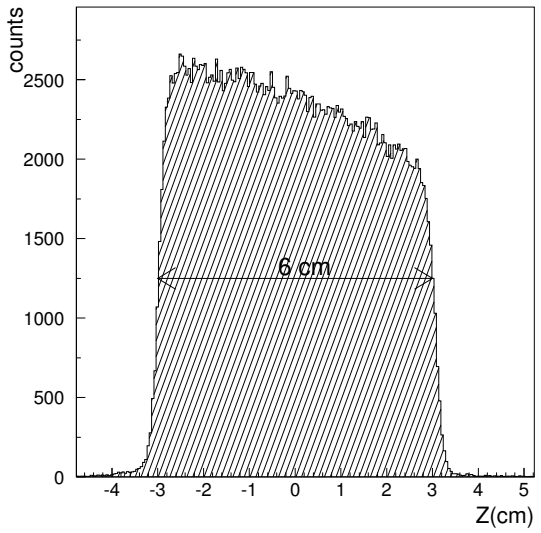

Fig. 8. Longitudinal target profile reconstructed from the vertex distribution of the $p\pi^+\pi^-$ reaction in the case of a 6 cm long target.

6 and 12 cm) have been used over the data taking periods. When filled with hydrogen, the working temperature is 18 K, giving a density $\rho \approx 7\ 10^{-2}$ g/cm^3.

The longitudinal position of the target is a crucial parameter for the control of the acceptance. The target profile displayed in fig. 8 corresponds to the vertex distribution (along the beam axis) of the three charged particles reaction $p\pi^+\pi^-$, provided by the central tracking detector (see sect. 2.4). From this distribution, the exact target position could be extracted. It should be noted that the profile shape reflects the geometrical acceptance of the central part of the detector for the selected events.

2.4 The LAγRANGE detector

The 4π LAγRANGE detector (fig. 1) has been designed to detect both neutral and charged particles produced in photoproduction reactions on light nuclei with total center-of-mass energy $W \leq 2$ GeV. The apparatus is composed of two main parts: a central one ($25^\circ \leq \theta \leq 155^\circ$) and a forward one ($\theta \leq 25^\circ$). In the following, all resolutions are given as Full Width Half-Maximum (FWHM).

Proton detection. The track of protons was measured by a set of Multi-Wire Proportional Chambers (MWPC). Two cylindrical chambers with stripped cathodes were used to cover the central region and gave a reconstruction efficiency $\geq 90\%$ with a resolution of 3.5° in θ and 4.5° in φ. The forward angles were measured by two planar chambers (efficiency $\geq 99\%$), each composed of two wire planes; the average polar and azimuthal resolutions were, respectively, 1.5° and 2°. Detailed discussions of the characteristics and performances of these detectors can be found in [17].

Particle identification was obtained by $\mathrm{d}E/\mathrm{d}x$ technique in the central region thanks to a plastic scintillator barrel (32 bars, 5 mm thick, 43 cm long and $\approx 20\%$ energy resolution) situated between the cylindrical chambers and the BGO calorimeter. For the more energetic particles emitted in the forward direction, a Time-of-Flight measurement was used, provided by a double plastic scintillator hodoscope ($300 \times 300 \times 3$ cm^3) placed at a distance of 3 m from the target and having a resolution of 600 ps. This latter detector provides also a measure of the energy loss.

For the cross-sections, due to large uncertainties on the cylindrical chambers efficiency, the proton direction was deduced from the association between the scintillator barrel and the BGO calorimeter (resolution $\sim 10^\circ$ in θ and φ).

γ-ray detection. The two γ-rays from the π^0 decay (branching ratio of 98.8%) were detected in the BGO calorimeter made of 480 ($15\theta \times 32\varphi$) crystals, each of 21 radiation lengths so that the associated electromagnetic shower was fully contained into the calorimeter. γ-rays were identified as clusters of adjacent crystals (3 on average for an energy threshold of 10 MeV per crystal) with no associated hit in the barrel. The measured photon energy resolution was 3% on average and the angular resolution was, respectively, 6° and 7° for polar and azimuthal angles ($E_\gamma \geq 200$ MeV and $l_{\mathrm{target}} = 3$ cm). The response of the BGO calorimeter has been investigated in numerous publications [18–20].

At forward angles, γ-rays can be detected in a lead-scintillator sandwich ToF wall [21] located behind the double plastic hodoscope. This detector provides a good angular resolution but no energy measurement and for the present reaction extends only marginally the covered angular range. For the sake of simplicity, it has not been used in the present analysis.

Backward angles ($\theta \geq 155^\circ$) are covered by a lead-scintillator sandwich disk not used in the present analysis.

2.5 Data acquisition and trigger

A specific data acquisition system [22] was used to collect the flow of events on DLT tapes at a typical rate of 200 events/s with a negligible dead time. Two main triggers were necessary for this experiment. The first one ("physical" events) was a coincidence between the "TAG" signal (see sect. 2.2.2) and an energy deposition larger than ~ 180 MeV in the BGO calorimeter. This open trigger allowed the simultaneous detection of all meson production channels over the covered energy range and was sufficient to reject the electromagnetic background generated in the target. The second one (monitor events), corresponding to the coincidence between the thin monitor and the "TAG" signals, was recorded in parallel with a downscaling factor of 1000. This latter trigger entered in the measurement of the integrated flux.

3 Data analysis

The results presented hereafter correspond to the summation of several data taking periods (nine spread over

four years) with sligthly different experimental conditions (laser wavelength, target length, plane chamber set-up, ...). More details can be found in [14].

3.1 Simulation

A complete simulation of the apparatus was developed using the GEANT3 code from the CERN library. This software includes the dependence of beam shape on energy and polarization, a realistic event generator [23] and a complete description of the different detection components of the LAγRANGE set-up (geometry and response). For each data taking period, a specific version adapted to the corresponding configuration was implemented.

In addition to the usual calculation of the efficiencies entering in the differential cross-section measurements, this simulation was an essential tool to determine the best set of selection cuts and their optimization *versus* background rejection and/or efficiency.

3.2 Tagging analysis

After checking that the correct information (TDC, ADC) for the hit plastics was available, only those events with one or two adjacent small plastics and a microstrip signal in geometrical coincidence were selected. This same selection criterion was applied to "physical" and monitor events.

3.3 Flux measurement

The flux measurement was based on a 32 bits scaler which counted the total number of coincidences, $N_{\rm scal}$, between the thin monitor and the "TAG" signals. The integrated beam flux has been calculated for each considered energy bin i using the following formula:

$$F(i) = N_{\rm scal} \frac{N^*_{\rm mon}(i)}{N_{\rm mon}} \frac{1}{\epsilon_{\rm mon}}\,, \qquad (8)$$

where $\epsilon_{\rm mon}$ is the intrinsic detection efficiency of the thin monitor, $N_{\rm mon}$ and $N^*_{\rm mon}$ are the numbers of thin monitor triggers before and after the event analysis, *i.e.* tagging analysis and selection of the "true" peak in the ToF spectrum (see fig. 9).

A typical ToF spectrum obtained for the thin monitor is shown in fig. 9. The peaks corresponding to the different electron bunches (separated by 2.8 ns) are clearly resolved. The contribution of accidental coincidences in the main peak is negligible ($< 0.15\%$).

3.4 Channel selection

Thanks to the 4π geometry of the LAγRANGE apparatus, all final-state particles were detected. The kinematics of this two-body reaction was therefore overdetermined. We

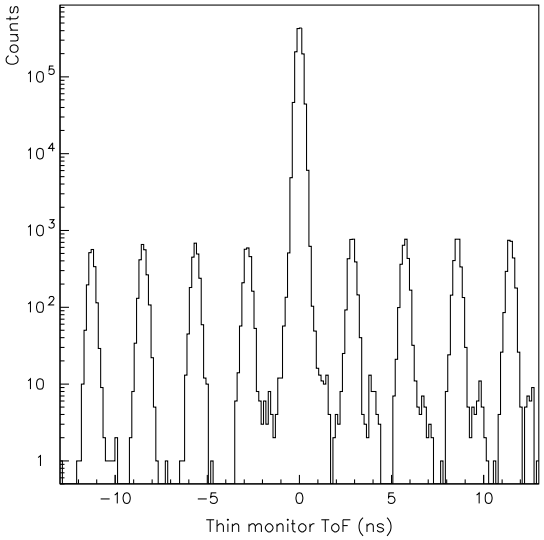

Fig. 9. Typical experimental Time-of-Flight spectrum for the thin monitor. The distance between two adjacent peaks is 2.8 ns. The level of accidental coincidences in the main peak is less than 0.15%.

took advantage of this characteristic to perform channel selection by means of kinematical cuts, in contrast to the usual background substraction method. The same method was applied for $\pi^0 p$ and ηp channels [24].

The first step of the analysis consisted in selecting events with only two neutral clusters in the BGO calorimeter and a single charged-particle track (see sect. 2.4). Cluster information was combined first to identify a π^0 by means of the usual invariant mass:

$$M_{\gamma\gamma} = \sqrt{2E_{\gamma 1}E_{\gamma 2}\left(1-\cos(\theta_{\gamma 1\gamma 2})\right)}\,, \qquad (9)$$

where $\theta_{\gamma 1\gamma 2}$ is the angle between the two decay photons, and, second, to reconstruct its direction (θ_{π^0}, φ_{π^0}) and energy E_{π^0}. After a cut on $M_{\gamma\gamma}$, we used the following set of selection cuts based on the two-body kinematics:

- $R_{\pi^0} = E_{\pi^0}/E^*_{\pi^0}$,
- $\Delta\theta_p = \theta^*_p - \theta_p$,
- $\Delta\varphi_p = \varphi^*_p - \varphi_p$,
- $\Delta t_p = {\rm ToF}^*_p - {\rm ToF}_p$ (only at forward angles),

where the "*" quantities were calculated from the kinematics using only two pieces of experimental information: the photon energy E_γ and the π^0 polar angle θ_{π^0}.

The experimental distributions of $M_{\gamma\gamma}$ are displayed in fig. 10 (closed circles). The upper spectrum shows the invariant mass after the first step of the analysis and the lower one after applying all selection cuts. One can see that the initial condition (two neutral clusters and one track) is already quite selective thanks to the 4π coverage of the apparatus. The latter spectrum is compared with the simulation of the $\pi^0 p$ reaction. The excellent agreement underlines the reliability of the simulation code and the low level of background (hadronic and electromagnetic).

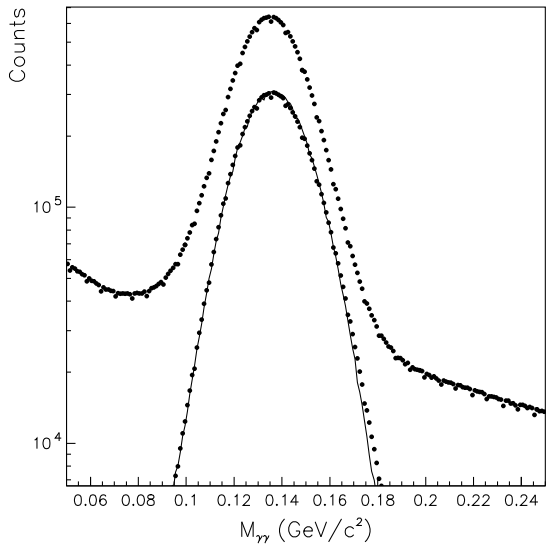

Fig. 10. π^0 invariant-mass spectrum. Data (closed circles) before and after all kinematical cuts are compared to simulation (solid line). See text for more details.

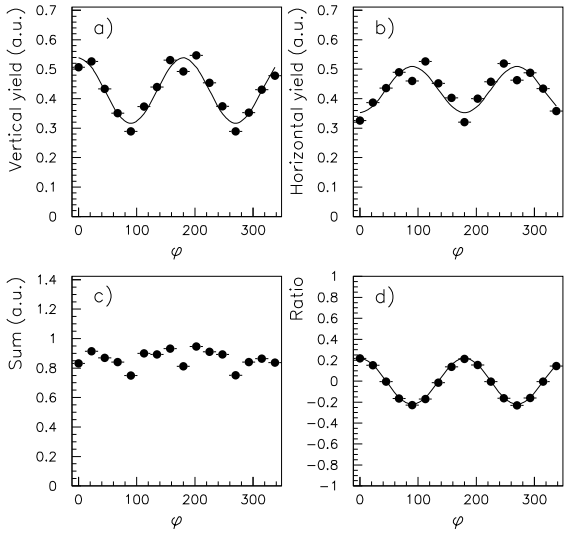

Fig. 11. Azimuthal normalized yields: a) vertical polarization; b) horizontal polarization; c) sum of a) and b) (eq. 13); d) ratio a)-b)/c) (eq. 14). The solid lines represent the fitted curves.

The small contribution of the hadronic background has been estimated with the simulation. Mainly composed of two-pions production ($\pi^+\pi^0 n$ and $\pi^0\pi^0 p$), it has been found below 1% over the whole tagged range. Contributions of the target cell have been measured with empty target runs and amount to 1.3% in accordance with the walls thickness. Finally, accidental coincidences have been found to be negligible ($< 0.1\%$).

3.5 Measurement of Σ

3.5.1 Method

For a linearly polarized beam with polarization P_γ, the differential cross-section at a given photon energy can be written as

$$\frac{\mathrm{d}\sigma}{\mathrm{d}\Omega}(\theta,\varphi) = \left(\frac{\mathrm{d}\sigma}{\mathrm{d}\Omega}(\theta)\right)_0 [1 + P_\gamma \Sigma(\theta)\cos 2(\varphi - \varphi_\gamma)], \quad (10)$$

where $(\mathrm{d}\sigma/\mathrm{d}\Omega)_0$ is the unpolarized differential cross-section, φ the azimuthal angle of the reaction plane and φ_γ the direction of the photon electric field. Alternating periods with vertical and horizontal polarization, we have obtained, for each energy and polar angular bin, the azimuthal yields normalized by the integrated flux, $\tilde{N}_\mathrm{V}$ and $\tilde{N}_\mathrm{H}$:

$$\tilde{N}_\mathrm{V}(\varphi) = \frac{N(\varphi, \varphi_\gamma = 90^\circ)}{F_\mathrm{V}} \quad (11a)$$

$$= \tilde{N}\epsilon_\mathrm{V}(\varphi)[1 + P_\gamma \Sigma \cos(2\varphi)]\,, \quad (11b)$$

$$\tilde{N}_\mathrm{H}(\varphi) = \frac{N(\varphi, \varphi_\gamma = 0^\circ)}{F_\mathrm{H}} \quad (12a)$$

$$= \tilde{N}\epsilon_\mathrm{H}(\varphi)[1 - P_\gamma \Sigma \cos(2\varphi)]\,, \quad (12b)$$

where $F_{\mathrm{V,H}}$ and $\epsilon_{\mathrm{V,H}}$ are the integrated flux and azimuthal efficiencies for the two polarization states, respectively. By combining eqs. (11b) and (12b) and assuming that $\epsilon(\varphi)$ does not depend on the state of polarization, we can then calculate the sum and the usual ratio:

$$\tilde{N}_\mathrm{V}(\varphi) + \tilde{N}_\mathrm{H}(\varphi) = \tilde{N}\epsilon(\varphi)\,, \quad (13)$$

$$\frac{\tilde{N}_\mathrm{V}(\varphi) - \tilde{N}_\mathrm{H}(\varphi)}{\tilde{N}_\mathrm{V}(\varphi) + \tilde{N}_\mathrm{H}(\varphi)} = P_\gamma \Sigma \cos(2\varphi)\,. \quad (14)$$

The experimental distributions corresponding to eqs. (11) to (14), summed over all energies and polar angles, are displayed in fig. 11. Thanks to the cylindrical symmetry of our set-up, the complete azimuthal distribution of events is observed and $\tilde{N}_\mathrm{V}$ as well as $\tilde{N}_\mathrm{H}$ exhibit the correct φ dependence (figs. 11a, b). The azimuthal acceptance is given by the sum spectrum (fig. 11c) which corresponds to the response of the apparatus to an unpolarized beam (same number of photons in the two orthogonal states); the observed anisotropies (of the order of 10%) are mostly due to the mechanical structure of the BGO calorimeter. As expected, the ratio (fig. 11d), from which the efficiency drops out, allows to get rid of most of the systematic errors as evidenced by an improved azimuthal distribution. Accordingly, we have fitted the ratio by the function $a\cos(2\varphi)$ (eq. 14) to extract $P_\gamma\Sigma$ and then Σ using the known energy dependence of P_γ. All reduced χ^2 values were found close to 1.

As mentioned earlier, we have implicitly assumed that the azimuthal efficiency $\epsilon(\varphi)$ is the same for both polarization states. This is not necessarily true since the beam shape is different for horizontal and vertical polarizations (see fig. 4). With the help of the detector simulation, we have investigated the effect of the vertex position on the azimuthal efficiency. We have found an efficiency variation

less than 1% whatever the transverse position and concluded that this is a negligible effect.

3.5.2 Corrections and errors

Among the various factors that can alter the measured asymmetries, only two were found non-negligible: the φ binning and the hadronic background. The first one tends to lower the true asymmetry and can be readily calculated whereas the latter one depends on the nature (asymmetry) of the background and has to be estimated by the simulation. Given the statistics and the φ resolution, the optimal φ binning was 16 ; the corresponding reduction factor R_φ was 2.6%. For the background contribution, we made the assumption of a zero asymmetry whatever the bin. In such a case, the correction factor is equal to the background/signal ratio R_b, which never exceeded 2%. The two corrections were combined as follows:

$$\Sigma_\mathrm{true} = \Sigma_\mathrm{meas}(1 + R_\varphi)(1 + R_\mathrm{b})\,. \qquad (15)$$

Two sources of systematical errors were considered: the uncertainty on the laser beam polarisation ($\delta\Sigma/\Sigma = 2.0\%$) and on the hadronic-background contributions ($\delta\Sigma \leq 0.02$). For this second one, we took into account an uncertainty on the amount of backgroung R_b and also on the assumed value of the background asymmetry. The absolute statistical uncertainty on Σ, given by the fitting procedure, was found in most cases lower than 0.03. All systematical and statistical errors have been summed quadratically.

3.5.3 Period comparison

Special care was taken to check the quality and stability of the analysis before merging data from the nine different periods. This was done first by monitoring the response of each detector of the GRAAL apparatus over the whole sample of selected events. The measured quantities (Σ and $\mathrm{d}\sigma/\mathrm{d}\Omega$) were also used to cross-check the various periods by calculating a χ^2 between each period and the global result. Despite the small error bars, the obtained reduced χ^2 were all found close to 1 and the final values of the beam asymmetry were extracted from the whole set of data.

Comparing results from green and UV periods allowed also to perform a crucial test on the energy dependence of the γ-ray beam polarization. As seen in fig. 7, below 1100 MeV, Σ could be measured with either of the two lines. The comparison, displayed in fig. 12, shows an excellent agreement and confirms that the beam polarization was well under control.

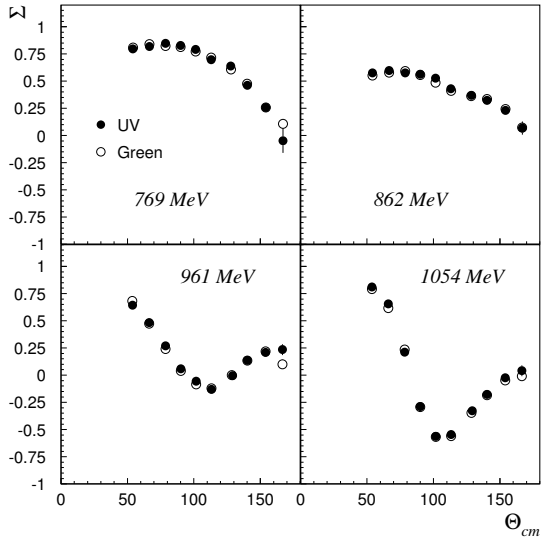

Fig. 12. Comparison of the beam asymmetry obtained for two laser lines for four energies in the overlapping region.

3.6 Measurement of $\mathrm{d}\sigma/\mathrm{d}\Omega$

3.6.1 Method

The differential cross-section for a given bin in energy E_γ and in $\cos\theta_\mathrm{cm}$, with θ_cm the π^0 center-of-mass angle, was calculated using the following expression:

$$\frac{\mathrm{d}\sigma}{\mathrm{d}\Omega}(\cos\theta_\mathrm{cm}, E_\gamma) = \frac{N(\cos\theta_\mathrm{cm}, E_\gamma)}{\epsilon(\cos\theta_\mathrm{cm}, E_\gamma)F(E_\gamma)\rho l \Delta\Omega}\,, \qquad (16)$$

where N is the number of selected events, ϵ the detection efficiency, F the integrated beam flux, ρ the hydrogen density, l the target length and $\Delta\Omega$ the solid angle corresponding to the chosen $\cos\theta_\mathrm{cm}$ binning (20 bins in the present case —$\Delta\Omega = 0.2\pi$). The values of ρ, l and F have been discussed previously (see sects. 2.3 and 3.3).

The detection efficiency ϵ has been derived from the simulation and was the most critical quantity in this formula. Applying broad cuts at $\pm 4\sigma$ on the five kinematical variables used for event selection, we obtained a global efficiency (including acceptance, detection, identification and selection) remaining larger than 45% over the whole energy range. To check the reliability of the simulation, a systematic comparison between experimental and simulated distributions of the different selection variables was performed. This comparison emphasized small discrepancies which have been attributed to imperfections of the simulation. Indeed, some details of the mechanical structure of the detector were not included and the associated efficiency losses have been estimated and eventually corrected.

The final cross-section values have been obtained after applying corrections for hadronic background ($\leq 2\%$, see sects. 3.4 and 3.5.2).

3.6.2 Systematical errors

Two types of systematical errors were taken into account: global normalization errors and bin-dependent errors. The global normalization error included the uncertainties on

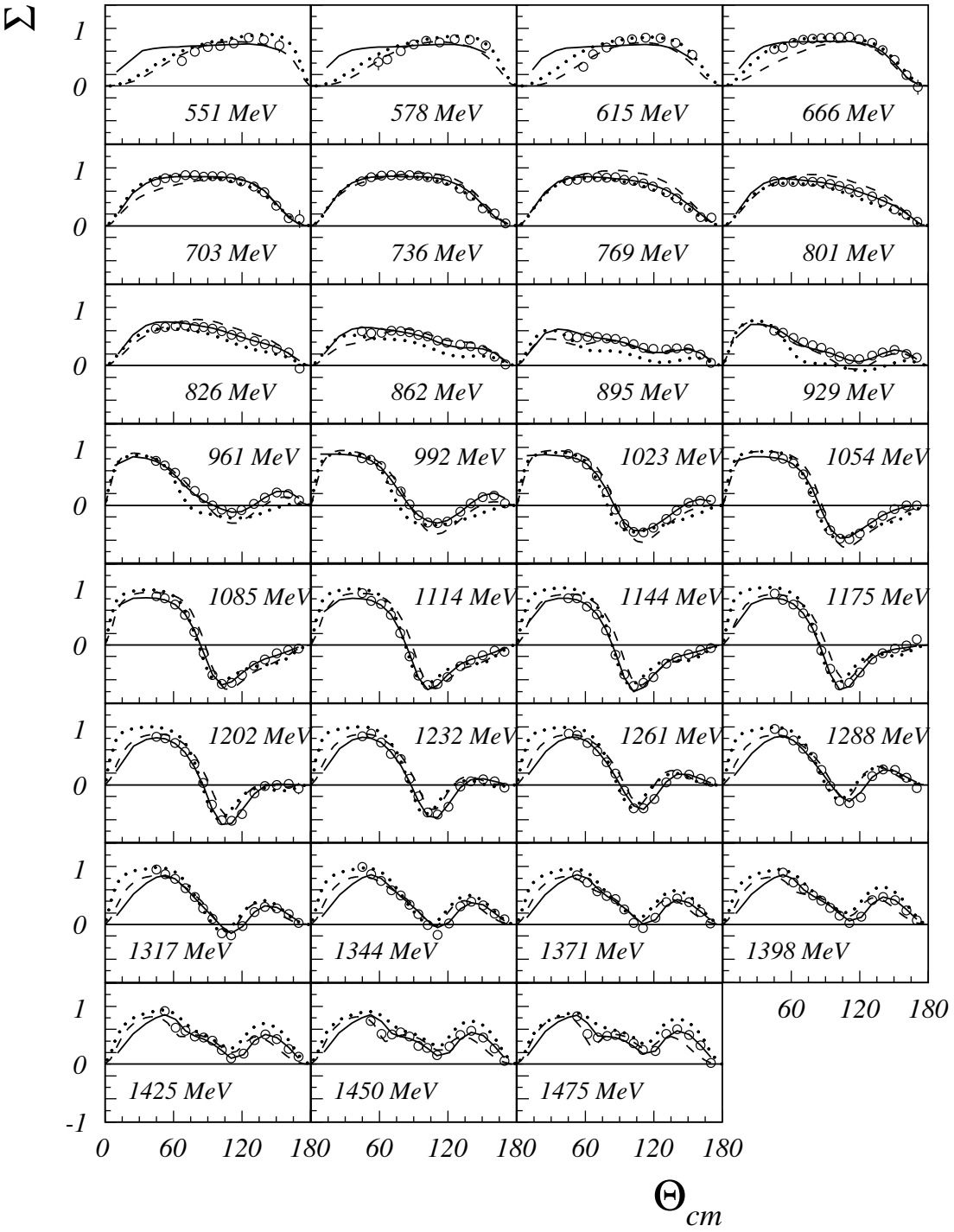

Fig. 13. Angular distributions of the beam asymmetry. Data are compared to the three models: SAID-FA04 (dashed line), MAID2005 (dotted line) and Bonn2005 (solid line).

the monitor efficiency, the hydrogen density and on the target length. The quadratic sum of these different contributions gave a global normalization error of 2.3%. The bin-dependent errors included uncertainties on the background contributions ($\leq 0.8\%$), the efficiency ($\leq 2\%$), the longitudinal target position (≤ 0.15 μb/sr) and on the geometrical corrections (2–4% for a few bins). These various bin-dependent contributions were summed quadratically with the statistical errors.

3.6.3 Period comparison

Differential cross-sections have been extracted from the same sample of selected runs as the beam asymmetry. A

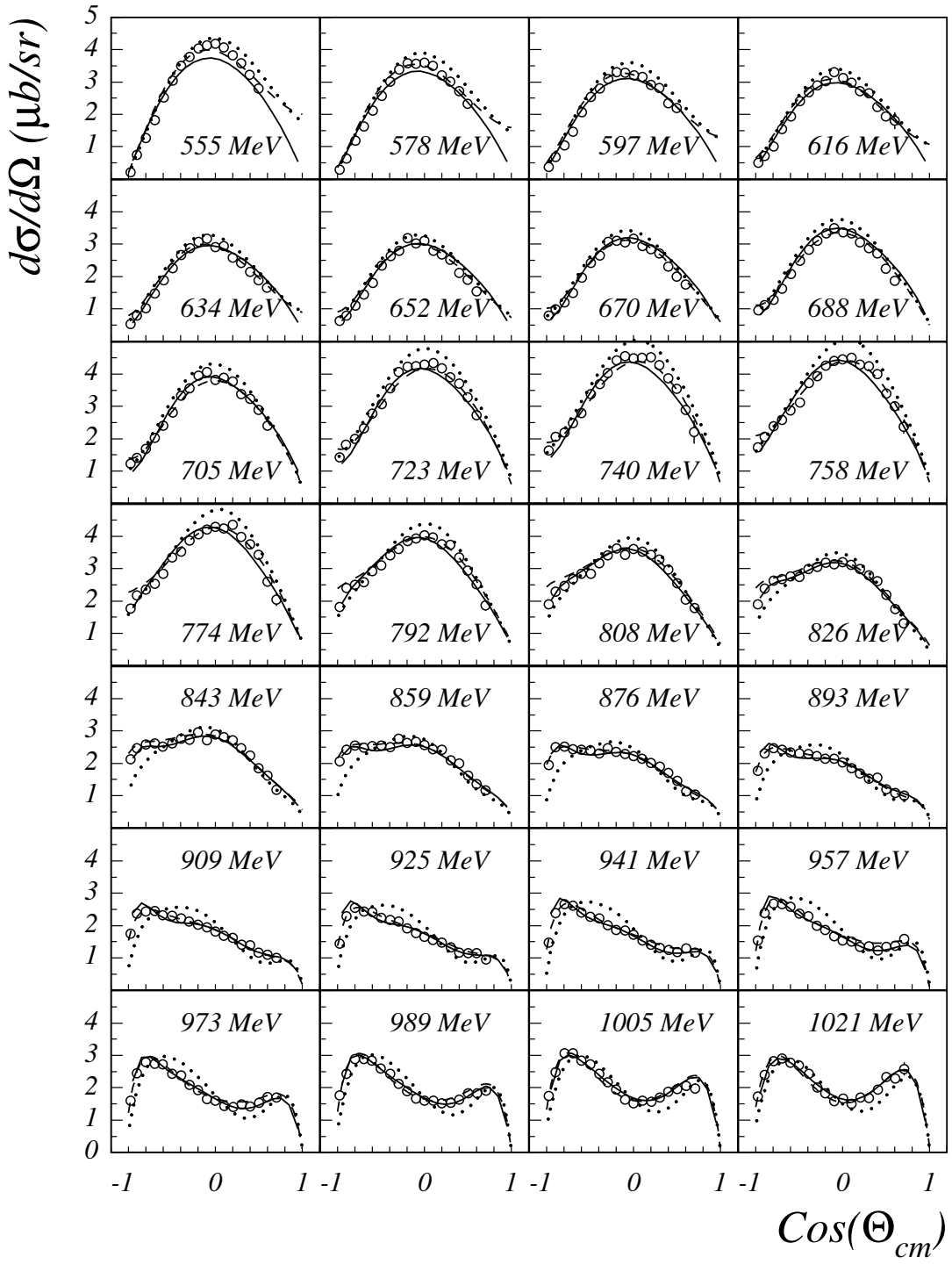

Fig. 14. Differential cross-sections for energies ranging from 555 MeV to 1021 MeV. Definition of the curves as in fig. 13.

similar χ^2 procedure was also used to test the compatibility of the different periods of data taking. Because $\mathrm{d}\sigma/\mathrm{d}\Omega$ is an absolute measurement, all factors that enter in the calculation must be precisely taken into account; this comparison, as well as the careful monitoring of the apparatus response, was therefore much more stringent than in the case of the asymmetry. Nevertheless, the obtained reduced χ^2 did not reveal any anomalous or bad period and the $\mathrm{d}\sigma/\mathrm{d}\Omega$ values have been extracted by summing up all periods.

4 Results and discussions

The complete set of asymmetry and differential cross-section data totalizing 1302 points is displayed in figs. 13

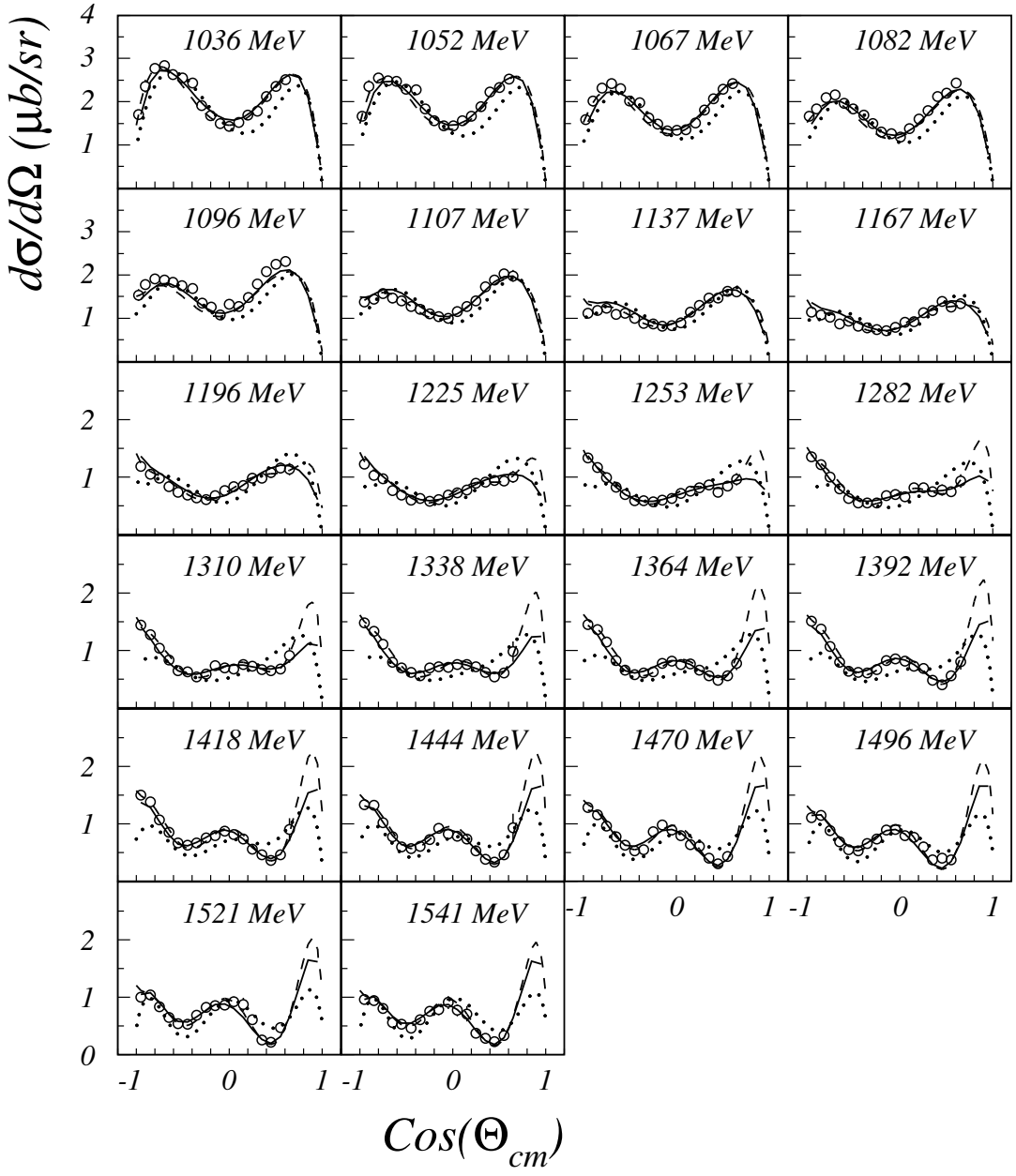

Fig. 15. Differential cross-sections for energies ranging from 1036 MeV to 1541 MeV. Curves as in fig. 14.

to 15. Numerical values are listed in tables 1 to 7. Error bars are the quadratic sum of statistical and systematical errors. For cross-sections, the global normalization uncertainty of 2.3% is not included. Data are available via internet [25].

4.1 Comparison with previous results

4.1.1 Beam asymmetry

Apart from a few data points obtained in the seventies, the only significant results concerning the beam asymmetry have been published by the Erevan group in the energy range 500–1100 MeV and for π^0 angles between 85 and 125° [26]. The comparison at four angles between Erevan (open circles) and GRAAL results (closed circles) is displayed in fig. 16. At first sight, the overall agreement between the two sets of data looks satisfactory. Nevertheless, looking in more detail, a small discrepancy is observed at 110 and 120° which is attributed to a shift in energy ($\Delta E \approx 15$ MeV) rather than to the beam polarization. Indeed, the shift remains constant over the whole energy range and in particular at the zero crossing where beam polarization is irrelevant. For the Erevan experiment, the photon energy was reconstructed from the kinematics of the proton in the magnetic spectrometer and different kinematic settings were used to cover the whole range. In our case, we used a tagged beam with one energy calibration and all angles were measured simultaneously in a 4π detector.

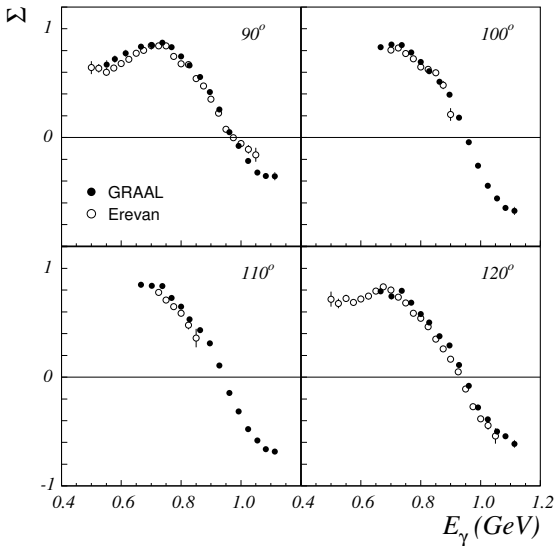

Fig. 16. Comparison between GRAAL (closed circles) and Erevan (open circles) beam asymmetries for four angles as a function of E_γ.

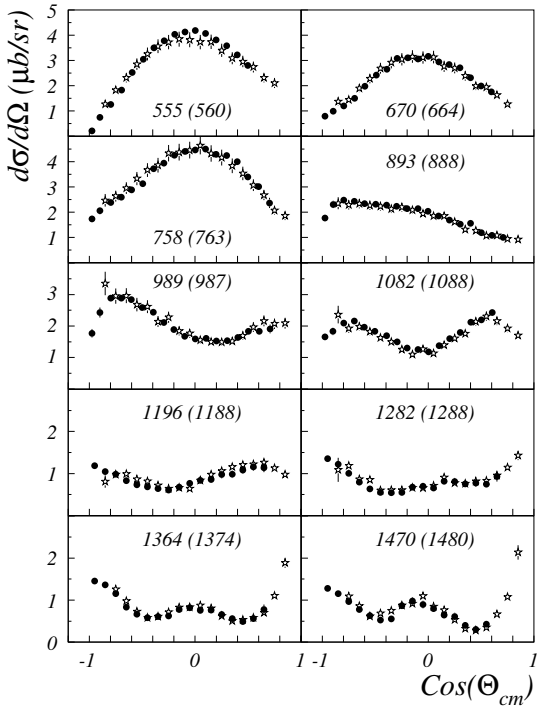

Fig. 17. Comparison between GRAAL (closed circles) and Bonn (stars) differential cross-sections for the closest energy bins of the two experiments. Energies are in MeV (Bonn values are in parenthesis).

4.1.2 Cross-section

Although less sparse than the beam asymmetry data, the differential cross-section database was limited until the recently published CB-ELSA results [27] which cover the energy range 0.3–3.0 GeV. The GRAAL data are absolute measurements including flux normalization in contrast to the Bonn results where the SAID partial-wave analysis was used for absolute normalization. The comparison between the GRAAL and Bonn data is shown in fig. 17 for the closest energy bins. The overall agreement is excellent over the whole range. It should be noted that our angular range is complementary to the Bonn one, extending the range to more backward angles.

4.2 Discussion

We have compared our results with three models (see figs. 13-15): the SAID partial-wave analysis (FA04, dashed line) [28,29], the unitary isobar model MAID (MAID 2005, dotted line) [30–32] and the recent coupled-channel partial-wave analysis developed at Bonn (solid line) [33, 34].

The SAID partial-wave analysis for pion photoproduction uses as database the total and differential cross-sections as well as the beam and target asymmetries for the $\pi^0 p$, $\pi^+ n$, $\pi^- n$ and $\pi^0 n$ channels up to 2 GeV. The FA04 solution [29] takes into account the Erevan beam asymmetries up to 1.1 GeV [26] and the recent Bonn differential cross-sections [27] for the $\pi^0 p$ reaction. The overall agreement is quite satisfactory especially for cross-sections. For the beam asymmetries (fig. 13), although the global trend is well reproduced, small discrepancies are observed for most energy bins.

MAID is a unitary isobar model designed to fit the pion photo- and electroproduction database. The model compared to our data is an extension of MAID2003 [30–32] which includes, for the $\pi^0 p$ channel, the latest Bonn cross-sections and the present GRAAL beam asymmetries. As seen in the figures, the new MAID2005 solution is able to well reproduce the whole set of data and largely improves the previous solution (not shown in the figures). In particular, all observed structures are now qualitatively described. An important impact of the new data was to impose an empirical correction on the high-energy tail for $\Delta(1232)P_{33}$ at $W > 1600$ MeV [31]. Further studies are being pursued to better understand the origin of this unexpected modification.

The Bonn coupled-channel PWA is a combined analysis of photoproduction experiments with πN, ηN, $K\Lambda$ and $K\Sigma$ final states [34]. As compared to the two previous models, it takes into account a larger database, with all polarization observable data, including our $\pi^0 p$ beam asymmetries. This approach is an important step towards a global analysis of the complete photoproduction database.

The agreement for both observables is excellent for all energies and angles except for the lowest-energy bins. More generally, a fair agreement with the whole database has been obtained with 14 N^* and 7 Δ^* resonances whose masses, widths and electromagnetic amplitudes are compatible with the PDG compilation. One of the main outcome of this model is the necessity to introduce several new resonances above 1800 MeV.

Table 1. Beam asymmetries for photon energies 551 MeV $\leq E_\gamma \leq$ 1023 MeV.

$\theta_{\rm cm}$ (°)	$E_\gamma = 551$ MeV	$\theta_{\rm cm}$ (°)	$E_\gamma = 578$ MeV	$\theta_{\rm cm}$ (°)	$E_\gamma = 615$ MeV
		59.3	0.417 ± 0.149	58.2	0.330 ± 0.068
67.4	0.431 ± 0.050	66.8	0.463 ± 0.034	66.9	0.546 ± 0.036
78.7	0.592 ± 0.041	78.8	0.601 ± 0.033	78.8	0.665 ± 0.033
89.9	0.670 ± 0.040	89.9	0.721 ± 0.032	89.9	0.774 ± 0.033
101.2	0.694 ± 0.044	101.2	0.783 ± 0.031	101.0	0.807 ± 0.033
112.9	0.736 ± 0.041	112.8	0.750 ± 0.035	112.8	0.835 ± 0.035
125.8	0.836 ± 0.049	125.9	0.810 ± 0.038	125.9	0.830 ± 0.037
139.1	0.796 ± 0.061	139.2	0.800 ± 0.047	139.2	0.743 ± 0.046
152.9	0.698 ± 0.119	153.1	0.696 ± 0.092	153.6	0.543 ± 0.079

$\theta_{\rm cm}$ (°)	$E_\gamma = 666$ MeV	$\theta_{\rm cm}$ (°)	$E_\gamma = 703$ MeV	$\theta_{\rm cm}$ (°)	$E_\gamma = 736$ MeV	$\theta_{\rm cm}$ (°)	$E_\gamma = 769$ MeV
44.7	0.634 ± 0.047	44.7	0.761 ± 0.033	44.7	0.769 ± 0.031	44.7	0.776 ± 0.028
52.8	0.661 ± 0.024	52.8	0.820 ± 0.027	52.7	0.842 ± 0.024	52.7	0.796 ± 0.024
61.7	0.743 ± 0.026	61.8	0.825 ± 0.023	61.7	0.863 ± 0.023	61.7	0.825 ± 0.021
70.4	0.801 ± 0.023	70.4	0.872 ± 0.026	70.4	0.873 ± 0.023	70.3	0.840 ± 0.021
78.6	0.821 ± 0.022	78.6	0.872 ± 0.023	78.6	0.865 ± 0.022	78.6	0.831 ± 0.023
86.3	0.824 ± 0.022	86.3	0.847 ± 0.024	86.3	0.873 ± 0.022	86.2	0.838 ± 0.023
94.0	0.837 ± 0.022	94.0	0.854 ± 0.024	94.0	0.866 ± 0.025	94.0	0.795 ± 0.022
102.2	0.844 ± 0.025	102.2	0.857 ± 0.025	102.2	0.839 ± 0.023	102.2	0.774 ± 0.022
110.8	0.854 ± 0.027	110.8	0.822 ± 0.024	110.8	0.814 ± 0.026	110.8	0.733 ± 0.020
119.3	0.811 ± 0.025	119.2	0.766 ± 0.027	119.2	0.773 ± 0.023	119.2	0.680 ± 0.023
130.7	0.748 ± 0.029	130.7	0.682 ± 0.023	130.6	0.639 ± 0.020	130.7	0.583 ± 0.020
139.7	0.622 ± 0.027	139.8	0.579 ± 0.021	139.9	0.515 ± 0.018	139.9	0.473 ± 0.018
150.2	0.447 ± 0.030	150.2	0.350 ± 0.025	150.3	0.306 ± 0.019	150.4	0.315 ± 0.018
161.0	0.186 ± 0.055	161.0	0.132 ± 0.043	160.9	0.210 ± 0.041	160.9	0.151 ± 0.026
170.7	−0.019 ± 0.133	170.5	0.115 ± 0.157	170.5	0.041 ± 0.083	170.5	0.138 ± 0.084
$\theta_{\rm cm}$ (°)	$E_\gamma = 801$ MeV	$\theta_{\rm cm}$ (°)	$E_\gamma = 826$ MeV	$\theta_{\rm cm}$ (°)	$E_\gamma = 862$ MeV	$\theta_{\rm cm}$ (°)	$E_\gamma = 895$ MeV
44.7	0.768 ± 0.029	44.8	0.633 ± 0.030	44.8	0.593 ± 0.029	44.8	0.515 ± 0.034
52.7	0.760 ± 0.021	52.8	0.660 ± 0.022	52.8	0.559 ± 0.028	52.7	0.481 ± 0.021
61.7	0.756 ± 0.021	61.7	0.685 ± 0.022	61.8	0.561 ± 0.023	61.7	0.490 ± 0.018
70.4	0.770 ± 0.023	70.4	0.691 ± 0.019	70.4	0.603 ± 0.018	70.4	0.497 ± 0.017
78.6	0.762 ± 0.021	78.6	0.668 ± 0.019	78.6	0.593 ± 0.019	78.6	0.468 ± 0.018
86.3	0.757 ± 0.021	86.3	0.664 ± 0.023	86.3	0.575 ± 0.020	86.3	0.460 ± 0.016
94.0	0.719 ± 0.020	94.0	0.636 ± 0.019	94.0	0.531 ± 0.018	94.0	0.415 ± 0.015
102.2	0.687 ± 0.020	102.2	0.591 ± 0.018	102.2	0.502 ± 0.016	102.3	0.371 ± 0.015
110.8	0.631 ± 0.021	110.8	0.527 ± 0.016	110.8	0.430 ± 0.016	110.9	0.302 ± 0.017
119.2	0.583 ± 0.019	119.2	0.493 ± 0.018	119.2	0.393 ± 0.017	119.3	0.287 ± 0.016
131.0	0.509 ± 0.019	131.0	0.426 ± 0.016	130.9	0.362 ± 0.015	130.9	0.281 ± 0.014
139.9	0.422 ± 0.015	140.0	0.370 ± 0.014	140.0	0.334 ± 0.014	140.0	0.294 ± 0.013
150.3	0.282 ± 0.016	150.4	0.284 ± 0.015	150.4	0.274 ± 0.014	150.4	0.285 ± 0.014
160.8	0.191 ± 0.036	160.8	0.227 ± 0.019	160.8	0.152 ± 0.018	160.7	0.185 ± 0.019
170.4	0.071 ± 0.083	170.4	−0.052 ± 0.060	170.4	0.020 ± 0.059	170.1	0.046 ± 0.081
$\theta_{\rm cm}$ (°)	$E_\gamma = 929$ MeV	$\theta_{\rm cm}$ (°)	$E_\gamma = 961$ MeV	$\theta_{\rm cm}$ (°)	$E_\gamma = 992$ MeV	$\theta_{\rm cm}$ (°)	$E_\gamma = 1023$ MeV
44.7	0.605 ± 0.028	44.8	0.767 ± 0.027	44.8	0.815 ± 0.027	44.9	0.881 ± 0.024
52.6	0.567 ± 0.020	52.5	0.688 ± 0.021	52.5	0.785 ± 0.022	52.5	0.823 ± 0.022
61.7	0.474 ± 0.019	61.5	0.562 ± 0.019	61.5	0.672 ± 0.021	61.5	0.701 ± 0.023
70.4	0.403 ± 0.017	70.3	0.401 ± 0.017	70.3	0.435 ± 0.016	70.2	0.511 ± 0.017
78.6	0.350 ± 0.018	78.6	0.244 ± 0.016	78.6	0.238 ± 0.017	78.5	0.231 ± 0.015
86.3	0.303 ± 0.017	86.4	0.119 ± 0.015	86.3	0.013 ± 0.014	86.3	−0.076 ± 0.015
94.1	0.223 ± 0.018	94.1	−0.003 ± 0.014	94.1	−0.169 ± 0.014	94.1	−0.329 ± 0.015
102.3	0.153 ± 0.014	102.3	−0.079 ± 0.014	102.4	−0.294 ± 0.015	102.4	−0.460 ± 0.017
110.9	0.110 ± 0.013	110.9	−0.127 ± 0.013	111.0	−0.305 ± 0.014	111.0	−0.470 ± 0.015
119.4	0.105 ± 0.015	119.5	−0.081 ± 0.014	119.6	−0.277 ± 0.015	119.7	−0.388 ± 0.016
130.8	0.168 ± 0.015	130.8	0.025 ± 0.012	130.7	−0.110 ± 0.014	130.7	−0.237 ± 0.013
140.0	0.229 ± 0.012	140.0	0.131 ± 0.011	140.0	0.034 ± 0.011	140.0	−0.097 ± 0.012
150.4	0.267 ± 0.013	150.3	0.217 ± 0.013	150.3	0.140 ± 0.012	150.3	0.039 ± 0.011
160.7	0.203 ± 0.018	160.6	0.193 ± 0.017	160.6	0.169 ± 0.016	160.6	0.075 ± 0.018
170.1	0.135 ± 0.074	170.2	0.083 ± 0.057	170.0	0.029 ± 0.059	169.8	0.098 ± 0.072

Table 2. Beam asymmetries for photon energies 1054 MeV $\leq E_\gamma \leq$ 1475 MeV.

$\theta_{\rm cm}$ (°)	$E_\gamma = 1054$ MeV	$\theta_{\rm cm}$ (°)	$E_\gamma = 1085$ MeV	$\theta_{\rm cm}$ (°)	$E_\gamma = 1114$ MeV	$\theta_{\rm cm}$ (°)	$E_\gamma = 1144$ MeV
44.9	0.843 ± 0.024	45.0	0.844 ± 0.029	45.0	0.894 ± 0.036	45.0	0.810 ± 0.041
52.5	0.805 ± 0.022	52.5	0.806 ± 0.023	52.7	0.765 ± 0.025	52.7	0.810 ± 0.026
61.5	0.720 ± 0.023	61.5	0.698 ± 0.019	61.5	0.712 ± 0.023	61.5	0.659 ± 0.024
70.2	0.535 ± 0.020	70.2	0.522 ± 0.020	70.1	0.516 ± 0.022	70.1	0.531 ± 0.025
78.5	0.228 ± 0.019	78.4	0.221 ± 0.019	78.4	0.202 ± 0.023	78.4	0.249 ± 0.025
86.3	−0.143 ± 0.016	86.2	−0.138 ± 0.017	86.2	−0.192 ± 0.024	86.2	−0.165 ± 0.029
94.1	−0.433 ± 0.017	94.1	−0.522 ± 0.022	94.0	−0.523 ± 0.025	94.0	−0.510 ± 0.027
102.4	−0.575 ± 0.018	102.4	−0.667 ± 0.019	102.3	−0.684 ± 0.031	102.4	−0.706 ± 0.029
111.0	−0.581 ± 0.018	111.0	−0.650 ± 0.019	110.9	−0.667 ± 0.023	110.9	−0.652 ± 0.025
119.9	−0.486 ± 0.020	119.9	−0.515 ± 0.021	119.6	−0.552 ± 0.027	119.7	−0.556 ± 0.031
130.6	−0.310 ± 0.015	130.7	−0.360 ± 0.015	130.9	−0.362 ± 0.019	130.9	−0.320 ± 0.023
140.0	−0.181 ± 0.013	140.0	−0.249 ± 0.016	140.0	−0.260 ± 0.016	140.1	−0.221 ± 0.016
150.4	−0.068 ± 0.013	150.4	−0.145 ± 0.013	150.4	−0.178 ± 0.016	150.6	−0.160 ± 0.018
160.7	−0.004 ± 0.015	160.8	−0.086 ± 0.016	160.9	−0.095 ± 0.025	161.0	−0.089 ± 0.023
169.9	−0.003 ± 0.054	169.8	−0.058 ± 0.053	169.8	−0.117 ± 0.079	169.8	−0.055 ± 0.080
$\theta_{\rm cm}$ (°)	$E_\gamma = 1175$ MeV	$\theta_{\rm cm}$ (°)	$E_\gamma = 1202$ MeV	$\theta_{\rm cm}$ (°)	$E_\gamma = 1232$ MeV	$\theta_{\rm cm}$ (°)	$E_\gamma = 1261$ MeV
45.1	0.886 ± 0.042	45.1	0.832 ± 0.045	45.2	0.839 ± 0.048	45.2	0.878 ± 0.049
52.7	0.783 ± 0.031	52.8	0.797 ± 0.030	52.8	0.881 ± 0.032	52.6	0.858 ± 0.031
61.6	0.700 ± 0.026	61.6	0.723 ± 0.027	61.6	0.725 ± 0.029	61.6	0.721 ± 0.031
70.2	0.544 ± 0.027	70.3	0.572 ± 0.027	70.2	0.532 ± 0.027	70.2	0.576 ± 0.028
78.4	0.299 ± 0.033	78.4	0.356 ± 0.027	78.5	0.446 ± 0.027	78.5	0.390 ± 0.028
86.1	−0.102 ± 0.041	86.2	0.029 ± 0.028	86.2	0.106 ± 0.030	86.2	0.191 ± 0.030
94.0	−0.406 ± 0.028	94.0	−0.348 ± 0.029	94.0	−0.197 ± 0.041	93.9	−0.106 ± 0.028
102.3	−0.693 ± 0.028	102.3	−0.614 ± 0.028	102.3	−0.480 ± 0.041	102.3	−0.411 ± 0.029
110.9	−0.649 ± 0.027	110.8	−0.617 ± 0.027	110.9	−0.515 ± 0.027	110.9	−0.404 ± 0.028
119.9	−0.477 ± 0.036	120.0	−0.503 ± 0.036	120.4	−0.383 ± 0.033	120.5	−0.243 ± 0.035
130.9	−0.252 ± 0.022	130.9	−0.147 ± 0.020	130.9	−0.032 ± 0.018	130.9	0.045 ± 0.018
140.1	−0.143 ± 0.016	140.1	−0.024 ± 0.016	140.2	0.063 ± 0.016	140.2	0.181 ± 0.015
150.6	−0.063 ± 0.017	150.6	−0.005 ± 0.018	150.7	0.093 ± 0.017	150.7	0.172 ± 0.016
160.9	−0.012 ± 0.024	161.0	0.016 ± 0.021	161.0	0.058 ± 0.020	161.0	0.106 ± 0.023
169.8	0.100 ± 0.079	169.7	−0.064 ± 0.097	169.7	−0.047 ± 0.078	169.7	0.053 ± 0.064
$\theta_{\rm cm}$ (°)	$E_\gamma = 1288$ MeV	$\theta_{\rm cm}$ (°)	$E_\gamma = 1317$ MeV	$\theta_{\rm cm}$ (°)	$E_\gamma = 1344$ MeV	$\theta_{\rm cm}$ (°)	$E_\gamma = 1371$ MeV
45.2	0.965 ± 0.051	45.3	0.949 ± 0.056	45.1	0.990 ± 0.069		
52.6	0.886 ± 0.037	52.7	0.865 ± 0.035	52.7	0.864 ± 0.039	52.5	0.846 ± 0.035
61.7	0.761 ± 0.030	61.6	0.790 ± 0.032	61.6	0.752 ± 0.044	61.7	0.722 ± 0.035
70.4	0.619 ± 0.028	70.4	0.622 ± 0.030	70.4	0.593 ± 0.034	70.5	0.568 ± 0.032
78.5	0.481 ± 0.028	78.6	0.477 ± 0.029	78.6	0.502 ± 0.030	78.7	0.495 ± 0.029
86.2	0.257 ± 0.031	86.2	0.282 ± 0.029	86.2	0.338 ± 0.028	86.3	0.440 ± 0.034
94.0	−0.026 ± 0.032	94.0	0.101 ± 0.028	94.0	0.175 ± 0.027	94.0	0.263 ± 0.032
102.2	−0.277 ± 0.028	102.1	−0.154 ± 0.028	102.2	−0.013 ± 0.027	102.1	0.025 ± 0.027
110.8	−0.314 ± 0.031	110.8	−0.190 ± 0.033	110.8	−0.178 ± 0.028	110.6	−0.060 ± 0.029
120.8	−0.220 ± 0.034	120.8	−0.024 ± 0.041	121.0	0.017 ± 0.035	121.1	0.115 ± 0.035
130.9	0.144 ± 0.018	130.9	0.218 ± 0.018	130.9	0.316 ± 0.018	130.9	0.386 ± 0.019
140.3	0.267 ± 0.018	140.3	0.304 ± 0.016	140.3	0.394 ± 0.016	140.3	0.444 ± 0.018
150.7	0.253 ± 0.017	150.7	0.281 ± 0.018	150.7	0.333 ± 0.020	150.8	0.382 ± 0.018
161.0	0.124 ± 0.019	161.0	0.178 ± 0.022	160.9	0.187 ± 0.018	161.0	0.211 ± 0.019
169.7	−0.058 ± 0.059	169.7	0.031 ± 0.070	169.8	0.093 ± 0.057	169.7	0.018 ± 0.056
$\theta_{\rm cm}$ (°)	$E_\gamma = 1398$ MeV	$\theta_{\rm cm}$ (°)	$E_\gamma = 1425$ MeV	$\theta_{\rm cm}$ (°)	$E_\gamma = 1450$ MeV	$\theta_{\rm cm}$ (°)	$E_\gamma = 1475$ MeV
52.6	0.894 ± 0.046	52.4	0.918 ± 0.039	52.4	0.744 ± 0.048	52.5	0.829 ± 0.051
61.6	0.722 ± 0.039	61.7	0.633 ± 0.038	61.8	0.518 ± 0.046	61.6	0.521 ± 0.075
70.6	0.615 ± 0.032	70.6	0.578 ± 0.034	70.7	0.514 ± 0.038	70.8	0.457 ± 0.045
78.8	0.498 ± 0.030	78.7	0.475 ± 0.034	78.8	0.552 ± 0.034	78.8	0.484 ± 0.036
86.3	0.409 ± 0.029	86.3	0.460 ± 0.031	86.3	0.481 ± 0.031	86.3	0.508 ± 0.033
94.0	0.284 ± 0.026	94.0	0.405 ± 0.032	94.0	0.321 ± 0.029	94.0	0.469 ± 0.031
102.1	0.155 ± 0.029	102.2	0.243 ± 0.026	102.1	0.279 ± 0.031	102.0	0.364 ± 0.033
110.7	0.028 ± 0.031	110.6	0.106 ± 0.029	110.5	0.157 ± 0.034	110.5	0.244 ± 0.037
121.3	0.138 ± 0.035	121.5	0.179 ± 0.044	121.5	0.308 ± 0.038	121.5	0.231 ± 0.044
130.9	0.418 ± 0.021	130.9	0.418 ± 0.019	130.9	0.501 ± 0.025	130.9	0.520 ± 0.023
140.4	0.473 ± 0.020	140.4	0.516 ± 0.020	140.4	0.578 ± 0.020	140.4	0.606 ± 0.021
150.7	0.423 ± 0.019	150.7	0.435 ± 0.020	150.7	0.461 ± 0.021	150.8	0.505 ± 0.022
161.0	0.241 ± 0.020	160.9	0.262 ± 0.021	160.9	0.273 ± 0.023	160.9	0.323 ± 0.025
169.7	0.072 ± 0.053	169.8	0.128 ± 0.063	169.7	0.057 ± 0.055	169.7	0.023 ± 0.077

Table 3. Differential cross-sections $d\sigma/d\Omega$ (μb/sr) for photon energies 555 MeV $\leq E_\gamma \leq$ 758 MeV.

$\cos(\theta_{cm})$	$E_\gamma = 555$ MeV	$\cos(\theta_{cm})$	$E_\gamma = 578$ MeV	$\cos(\theta_{cm})$	$E_\gamma = 597$ MeV	$\cos(\theta_{cm})$	$E_\gamma = 616$ MeV
−0.97	0.208 ± 0.048	−0.98	0.294 ± 0.057	−0.98	0.376 ± 0.063	−0.97	0.505 ± 0.073
−0.90	0.744 ± 0.061	−0.90	0.634 ± 0.059	−0.90	0.677 ± 0.058	−0.90	0.710 ± 0.057
−0.80	1.257 ± 0.052	−0.80	1.190 ± 0.053	−0.80	1.034 ± 0.050	−0.80	1.000 ± 0.048
−0.69	1.818 ± 0.059	−0.70	1.617 ± 0.067	−0.70	1.464 ± 0.057	−0.70	1.534 ± 0.054
−0.59	2.517 ± 0.073	−0.59	2.113 ± 0.071	−0.60	2.068 ± 0.072	−0.59	1.926 ± 0.069
−0.49	3.040 ± 0.080	−0.49	2.562 ± 0.083	−0.49	2.530 ± 0.077	−0.49	2.409 ± 0.076
−0.39	3.500 ± 0.075	−0.39	3.014 ± 0.076	−0.39	2.795 ± 0.074	−0.39	2.675 ± 0.074
−0.29	3.778 ± 0.078	−0.29	3.381 ± 0.087	−0.29	3.086 ± 0.082	−0.29	2.901 ± 0.075
−0.19	4.029 ± 0.083	−0.19	3.582 ± 0.084	−0.19	3.300 ± 0.080	−0.19	3.027 ± 0.076
−0.10	4.130 ± 0.077	−0.10	3.569 ± 0.095	−0.10	3.289 ± 0.083	−0.10	3.308 ± 0.096
0.00	4.179 ± 0.088	0.00	3.601 ± 0.095	0.00	3.207 ± 0.087	0.00	3.122 ± 0.087
0.10	4.063 ± 0.082	0.10	3.498 ± 0.091	0.10	3.152 ± 0.081	0.10	2.979 ± 0.080
0.20	3.815 ± 0.075	0.20	3.206 ± 0.085	0.20	2.916 ± 0.075	0.20	2.712 ± 0.074
0.30	3.576 ± 0.070	0.30	3.015 ± 0.080	0.30	2.808 ± 0.075	0.30	2.647 ± 0.076
0.40	3.215 ± 0.066	0.40	2.718 ± 0.078	0.40	2.335 ± 0.069	0.40	2.226 ± 0.070
0.50	2.797 ± 0.104	0.50	2.319 ± 0.082	0.50	2.197 ± 0.077	0.50	1.925 ± 0.063
						0.60	1.806 ± 0.259
$\cos(\theta_{cm})$	$E_\gamma = 634$ MeV	$\cos(\theta_{cm})$	$E_\gamma = 652$ MeV	$\cos(\theta_{cm})$	$E_\gamma = 670$ MeV	$\cos(\theta_{cm})$	$E_\gamma = 688$ MeV
−0.98	0.529 ± 0.076	−0.98	0.622 ± 0.083	−0.98	0.793 ± 0.090	−0.97	0.949 ± 0.102
−0.90	0.797 ± 0.061	−0.90	0.795 ± 0.062	−0.90	0.991 ± 0.072	−0.90	1.113 ± 0.082
−0.80	1.021 ± 0.047	−0.80	1.103 ± 0.046	−0.80	1.195 ± 0.044	−0.80	1.285 ± 0.051
−0.70	1.471 ± 0.056	−0.69	1.447 ± 0.052	−0.69	1.497 ± 0.054	−0.70	1.623 ± 0.058
−0.60	1.887 ± 0.066	−0.60	1.797 ± 0.072	−0.60	1.969 ± 0.071	−0.60	2.077 ± 0.074
−0.49	2.264 ± 0.081	−0.49	2.338 ± 0.085	−0.49	2.417 ± 0.076	−0.49	2.483 ± 0.085
−0.39	2.661 ± 0.077	−0.39	2.640 ± 0.074	−0.39	2.654 ± 0.080	−0.39	2.821 ± 0.091
−0.29	2.883 ± 0.078	−0.29	2.794 ± 0.084	−0.29	3.073 ± 0.084	−0.29	3.107 ± 0.103
−0.19	3.076 ± 0.079	−0.19	3.194 ± 0.085	−0.19	3.101 ± 0.092	−0.19	3.337 ± 0.098
−0.10	3.164 ± 0.096	−0.09	3.030 ± 0.090	−0.10	3.051 ± 0.093	−0.10	3.497 ± 0.106
0.00	2.902 ± 0.081	0.00	3.113 ± 0.095	0.00	3.163 ± 0.083	0.00	3.371 ± 0.095
0.10	2.940 ± 0.083	0.10	2.800 ± 0.084	0.10	2.942 ± 0.080	0.10	3.329 ± 0.101
0.20	2.582 ± 0.077	0.20	2.683 ± 0.075	0.20	2.838 ± 0.080	0.20	3.054 ± 0.095
0.30	2.420 ± 0.073	0.30	2.512 ± 0.075	0.30	2.707 ± 0.076	0.30	2.874 ± 0.080
0.40	2.150 ± 0.067	0.40	2.115 ± 0.066	0.40	2.308 ± 0.077	0.40	2.712 ± 0.084
0.50	1.890 ± 0.063	0.50	1.902 ± 0.065	0.50	1.990 ± 0.069	0.50	2.237 ± 0.084
0.60	1.654 ± 0.119	0.60	1.544 ± 0.087	0.60	1.758 ± 0.084	0.60	1.873 ± 0.083
$\cos(\theta_{cm})$	$E_\gamma = 705$ MeV	$\cos(\theta_{cm})$	$E_\gamma = 723$ MeV	$\cos(\theta_{cm})$	$E_\gamma = 740$ MeV	$\cos(\theta_{cm})$	$E_\gamma = 758$ MeV
−0.98	1.228 ± 0.114	−0.98	1.431 ± 0.118	−0.98	1.642 ± 0.128	−0.98	1.734 ± 0.122
−0.90	1.412 ± 0.099	−0.90	1.818 ± 0.121	−0.90	2.067 ± 0.133	−0.90	2.055 ± 0.133
−0.80	1.694 ± 0.059	−0.80	1.991 ± 0.059	−0.80	2.196 ± 0.061	−0.80	2.380 ± 0.062
−0.70	2.023 ± 0.063	−0.70	2.323 ± 0.062	−0.70	2.477 ± 0.061	−0.70	2.590 ± 0.059
−0.60	2.400 ± 0.078	−0.60	2.781 ± 0.078	−0.60	2.789 ± 0.080	−0.60	2.878 ± 0.074
−0.49	2.808 ± 0.091	−0.49	3.079 ± 0.090	−0.49	3.373 ± 0.100	−0.49	3.123 ± 0.085
−0.39	3.333 ± 0.097	−0.39	3.556 ± 0.091	−0.39	3.694 ± 0.089	−0.39	3.725 ± 0.093
−0.29	3.565 ± 0.101	−0.29	4.061 ± 0.092	−0.29	4.031 ± 0.094	−0.29	3.942 ± 0.096
−0.19	3.958 ± 0.102	−0.19	4.232 ± 0.102	−0.19	4.428 ± 0.100	−0.19	4.256 ± 0.091
−0.10	4.067 ± 0.104	−0.10	4.251 ± 0.097	−0.10	4.547 ± 0.100	−0.10	4.407 ± 0.100
0.00	3.828 ± 0.102	0.00	4.299 ± 0.100	0.00	4.485 ± 0.100	0.00	4.461 ± 0.102
0.10	3.887 ± 0.101	0.10	4.344 ± 0.102	0.10	4.503 ± 0.093	0.10	4.503 ± 0.101
0.20	3.765 ± 0.100	0.20	4.175 ± 0.098	0.20	4.524 ± 0.097	0.20	4.291 ± 0.096
0.30	3.385 ± 0.093	0.30	3.904 ± 0.093	0.30	4.285 ± 0.098	0.30	4.239 ± 0.092
0.40	3.229 ± 0.087	0.40	3.709 ± 0.092	0.40	3.878 ± 0.091	0.40	3.996 ± 0.093
0.50	2.900 ± 0.091	0.50	3.281 ± 0.092	0.50	3.550 ± 0.091	0.50	3.396 ± 0.088
0.60	2.411 ± 0.095	0.60	2.726 ± 0.091	0.60	2.893 ± 0.097	0.60	3.007 ± 0.095
				0.70	2.208 ± 0.363	0.70	2.363 ± 0.204

Table 4. Differential cross-sections $d\sigma/d\Omega$ (μb/sr) for photon energies 774 MeV $\leq E_\gamma \leq$ 957 MeV.

$\cos(\theta_{cm})$	$E_\gamma = 774$ MeV	$\cos(\theta_{cm})$	$E_\gamma = 792$ MeV	$\cos(\theta_{cm})$	$E_\gamma = 808$ MeV	$\cos(\theta_{cm})$	$E_\gamma = 826$ MeV
−0.98	1.763 ± 0.138	−0.98	1.810 ± 0.127	−0.98	1.892 ± 0.144	−0.98	1.889 ± 0.129
−0.90	2.174 ± 0.142	−0.90	2.401 ± 0.153	−0.90	2.295 ± 0.143	−0.90	2.381 ± 0.151
−0.80	2.353 ± 0.063	−0.80	2.498 ± 0.061	−0.80	2.475 ± 0.063	−0.80	2.628 ± 0.060
−0.70	2.534 ± 0.062	−0.70	2.577 ± 0.059	−0.70	2.678 ± 0.056	−0.70	2.675 ± 0.054
−0.60	2.835 ± 0.079	−0.60	2.918 ± 0.078	−0.60	2.835 ± 0.068	−0.60	2.758 ± 0.066
−0.49	3.347 ± 0.094	−0.50	3.098 ± 0.086	−0.49	2.835 ± 0.088	−0.50	2.741 ± 0.079
−0.39	3.519 ± 0.096	−0.39	3.409 ± 0.094	−0.39	3.165 ± 0.086	−0.39	2.995 ± 0.080
−0.29	3.877 ± 0.104	−0.30	3.614 ± 0.092	−0.30	3.416 ± 0.099	−0.29	3.057 ± 0.085
−0.19	4.071 ± 0.101	−0.20	3.848 ± 0.097	−0.20	3.620 ± 0.101	−0.20	3.191 ± 0.099
−0.10	4.216 ± 0.110	−0.10	3.928 ± 0.107	−0.10	3.427 ± 0.102	−0.10	3.129 ± 0.097
0.00	4.288 ± 0.102	0.00	4.029 ± 0.106	0.00	3.602 ± 0.107	0.00	3.197 ± 0.097
0.10	4.239 ± 0.100	0.10	3.972 ± 0.101	0.10	3.532 ± 0.100	0.10	3.113 ± 0.099
0.20	4.364 ± 0.104	0.20	3.763 ± 0.107	0.20	3.434 ± 0.098	0.20	2.981 ± 0.084
0.30	3.987 ± 0.107	0.30	3.736 ± 0.104	0.30	3.283 ± 0.096	0.30	2.788 ± 0.093
0.40	3.763 ± 0.100	0.40	3.348 ± 0.098	0.40	2.974 ± 0.092	0.40	2.619 ± 0.083
0.50	3.423 ± 0.103	0.50	2.932 ± 0.093	0.50	2.541 ± 0.089	0.50	2.193 ± 0.081
0.60	2.598 ± 0.100	0.60	2.522 ± 0.092	0.60	2.049 ± 0.085	0.60	1.752 ± 0.076
0.70	2.046 ± 0.194	0.70	1.862 ± 0.155	0.70	1.781 ± 0.141	0.70	1.311 ± 0.108
$\cos(\theta_{cm})$	$E_\gamma = 843$ MeV	$\cos(\theta_{cm})$	$E_\gamma = 859$ MeV	$\cos(\theta_{cm})$	$E_\gamma = 876$ MeV	$\cos(\theta_{cm})$	$E_\gamma = 893$ MeV
−0.98	2.128 ± 0.140	−0.98	2.054 ± 0.153	−0.98	1.952 ± 0.147	−0.98	1.771 ± 0.130
−0.90	2.465 ± 0.154	−0.90	2.422 ± 0.153	−0.90	2.496 ± 0.157	−0.90	2.304 ± 0.146
−0.80	2.583 ± 0.062	−0.80	2.547 ± 0.061	−0.80	2.514 ± 0.061	−0.80	2.472 ± 0.059
−0.70	2.616 ± 0.054	−0.70	2.487 ± 0.054	−0.70	2.438 ± 0.051	−0.70	2.425 ± 0.051
−0.60	2.511 ± 0.065	−0.60	2.532 ± 0.062	−0.60	2.419 ± 0.062	−0.60	2.335 ± 0.060
−0.50	2.615 ± 0.075	−0.50	2.541 ± 0.072	−0.50	2.403 ± 0.076	−0.50	2.307 ± 0.069
−0.39	2.762 ± 0.075	−0.39	2.501 ± 0.073	−0.39	2.302 ± 0.066	−0.39	2.283 ± 0.067
−0.30	2.730 ± 0.077	−0.30	2.761 ± 0.077	−0.30	2.461 ± 0.076	−0.30	2.226 ± 0.070
−0.20	2.961 ± 0.085	−0.20	2.625 ± 0.082	−0.20	2.345 ± 0.078	−0.20	2.139 ± 0.074
−0.10	2.718 ± 0.087	−0.10	2.658 ± 0.078	−0.10	2.288 ± 0.077	−0.10	2.136 ± 0.080
0.00	2.884 ± 0.085	0.00	2.558 ± 0.087	0.00	2.226 ± 0.079	0.00	2.030 ± 0.082
0.10	2.807 ± 0.090	0.10	2.438 ± 0.079	0.10	2.144 ± 0.078	0.10	1.843 ± 0.073
0.20	2.703 ± 0.084	0.20	2.419 ± 0.089	0.20	2.004 ± 0.078	0.20	1.682 ± 0.064
0.30	2.468 ± 0.081	0.30	2.089 ± 0.079	0.30	1.888 ± 0.072	0.30	1.526 ± 0.063
0.40	2.241 ± 0.081	0.40	2.001 ± 0.072	0.40	1.696 ± 0.068	0.40	1.560 ± 0.060
0.50	1.847 ± 0.072	0.50	1.627 ± 0.066	0.50	1.461 ± 0.062	0.50	1.189 ± 0.052
0.60	1.615 ± 0.069	0.60	1.361 ± 0.062	0.60	1.137 ± 0.056	0.60	1.075 ± 0.049
0.70	1.173 ± 0.098	0.71	1.163 ± 0.095	0.71	1.031 ± 0.089	0.71	1.002 ± 0.085
$\cos(\theta_{cm})$	$E_\gamma = 909$ MeV	$\cos(\theta_{cm})$	$E_\gamma = 925$ MeV	$\cos(\theta_{cm})$	$E_\gamma = 941$ MeV	$\cos(\theta_{cm})$	$E_\gamma = 957$ MeV
−0.98	1.741 ± 0.137	−0.98	1.433 ± 0.107	−0.98	1.471 ± 0.117	−0.98	1.535 ± 0.122
−0.90	2.363 ± 0.148	−0.90	2.293 ± 0.150	−0.90	2.379 ± 0.152	−0.90	2.376 ± 0.152
−0.80	2.440 ± 0.063	−0.80	2.555 ± 0.063	−0.80	2.658 ± 0.064	−0.80	2.671 ± 0.064
−0.70	2.448 ± 0.051	−0.70	2.429 ± 0.050	−0.70	2.610 ± 0.054	−0.70	2.659 ± 0.053
−0.60	2.324 ± 0.059	−0.60	2.419 ± 0.056	−0.60	2.393 ± 0.057	−0.60	2.577 ± 0.063
−0.50	2.298 ± 0.074	−0.50	2.236 ± 0.073	−0.50	2.273 ± 0.069	−0.50	2.366 ± 0.074
−0.39	2.214 ± 0.065	−0.39	2.166 ± 0.064	−0.39	2.224 ± 0.070	−0.39	2.278 ± 0.069
−0.30	2.126 ± 0.063	−0.30	2.117 ± 0.068	−0.30	2.004 ± 0.069	−0.30	1.992 ± 0.064
−0.20	2.021 ± 0.070	−0.20	1.916 ± 0.068	−0.20	1.870 ± 0.063	−0.20	1.861 ± 0.072
−0.10	1.939 ± 0.064	−0.10	1.765 ± 0.066	−0.10	1.849 ± 0.069	−0.10	1.673 ± 0.067
0.00	1.814 ± 0.066	0.00	1.645 ± 0.071	0.00	1.708 ± 0.066	0.00	1.537 ± 0.064
0.10	1.690 ± 0.065	0.10	1.553 ± 0.064	0.10	1.540 ± 0.070	0.10	1.504 ± 0.063
0.20	1.619 ± 0.062	0.20	1.475 ± 0.064	0.20	1.413 ± 0.060	0.20	1.333 ± 0.059
0.30	1.401 ± 0.061	0.30	1.332 ± 0.056	0.30	1.312 ± 0.054	0.30	1.354 ± 0.058
0.40	1.393 ± 0.060	0.40	1.160 ± 0.052	0.40	1.237 ± 0.050	0.40	1.226 ± 0.054
0.50	1.157 ± 0.050	0.50	1.144 ± 0.051	0.50	1.175 ± 0.051	0.50	1.344 ± 0.057
0.60	1.091 ± 0.053	0.60	1.148 ± 0.053	0.60	1.285 ± 0.057	0.60	1.374 ± 0.065
0.71	0.996 ± 0.088	0.71	0.943 ± 0.092	0.71	1.160 ± 0.106	0.71	1.578 ± 0.125

Table 5. Differential cross-sections $\mathrm{d}\sigma/\mathrm{d}\Omega$ (μb/sr) for photon energies 973 MeV $\leq E_\gamma \leq$ 1096 MeV.

$\cos(\theta_{\mathrm{cm}})$	$E_\gamma = 973$ MeV	$\cos(\theta_{\mathrm{cm}})$	$E_\gamma = 989$ MeV	$\cos(\theta_{\mathrm{cm}})$	$E_\gamma = 1005$ MeV	$\cos(\theta_{\mathrm{cm}})$	$E_\gamma = 1021$ MeV
−0.98	1.602 ± 0.124	−0.98	1.769 ± 0.134	−0.98	1.753 ± 0.122	−0.98	1.724 ± 0.122
−0.90	2.456 ± 0.158	−0.90	2.428 ± 0.154	−0.90	2.473 ± 0.161	−0.90	2.399 ± 0.151
−0.80	2.787 ± 0.067	−0.80	2.881 ± 0.072	−0.80	3.063 ± 0.074	−0.80	2.821 ± 0.072
−0.70	2.739 ± 0.053	−0.70	2.882 ± 0.055	−0.70	3.063 ± 0.053	−0.70	2.900 ± 0.053
−0.60	2.733 ± 0.063	−0.60	2.833 ± 0.067	−0.60	2.846 ± 0.063	−0.60	2.775 ± 0.059
−0.50	2.428 ± 0.073	−0.50	2.587 ± 0.080	−0.50	2.721 ± 0.086	−0.50	2.685 ± 0.082
−0.39	2.385 ± 0.076	−0.39	2.438 ± 0.083	−0.39	2.435 ± 0.082	−0.39	2.432 ± 0.078
−0.30	2.092 ± 0.069	−0.30	2.116 ± 0.072	−0.30	2.165 ± 0.068	−0.29	2.015 ± 0.076
−0.20	1.921 ± 0.071	−0.20	1.892 ± 0.070	−0.20	1.950 ± 0.075	−0.20	1.828 ± 0.075
−0.10	1.651 ± 0.066	−0.10	1.671 ± 0.068	−0.10	1.640 ± 0.071	−0.10	1.587 ± 0.073
0.00	1.601 ± 0.062	0.00	1.593 ± 0.064	0.00	1.521 ± 0.068	0.00	1.658 ± 0.071
0.10	1.437 ± 0.059	0.10	1.608 ± 0.063	0.10	1.595 ± 0.062	0.10	1.506 ± 0.065
0.20	1.403 ± 0.060	0.20	1.522 ± 0.060	0.20	1.569 ± 0.072	0.20	1.694 ± 0.071
0.30	1.491 ± 0.061	0.30	1.533 ± 0.064	0.30	1.700 ± 0.070	0.30	1.688 ± 0.063
0.40	1.420 ± 0.059	0.40	1.638 ± 0.065	0.40	1.870 ± 0.072	0.40	1.945 ± 0.075
0.50	1.541 ± 0.060	0.50	1.831 ± 0.065	0.50	1.959 ± 0.070	0.50	2.341 ± 0.078
0.60	1.718 ± 0.069	0.61	1.830 ± 0.073	0.61	2.060 ± 0.077	0.61	2.283 ± 0.088
0.71	1.703 ± 0.139	0.71	1.905 ± 0.138	0.71	1.970 ± 0.161	0.71	2.581 ± 0.204
$\cos(\theta_{\mathrm{cm}})$	$E_\gamma = 1036$ MeV	$\cos(\theta_{\mathrm{cm}})$	$E_\gamma = 1052$ MeV	$\cos(\theta_{\mathrm{cm}})$	$E_\gamma = 1067$ MeV	$\cos(\theta_{\mathrm{cm}})$	$E_\gamma = 1082$ MeV
−0.98	1.708 ± 0.118	−0.98	1.662 ± 0.112	−0.98	1.579 ± 0.108	−0.98	1.658 ± 0.107
−0.90	2.355 ± 0.150	−0.90	2.350 ± 0.146	−0.90	2.010 ± 0.127	−0.90	1.829 ± 0.114
−0.80	2.766 ± 0.069	−0.80	2.552 ± 0.066	−0.80	2.316 ± 0.064	−0.80	2.096 ± 0.060
−0.70	2.831 ± 0.055	−0.70	2.480 ± 0.050	−0.70	2.416 ± 0.048	−0.70	2.159 ± 0.051
−0.60	2.633 ± 0.060	−0.60	2.468 ± 0.057	−0.60	2.297 ± 0.059	−0.60	1.964 ± 0.054
−0.50	2.554 ± 0.078	−0.50	2.293 ± 0.083	−0.50	2.010 ± 0.071	−0.50	1.834 ± 0.062
−0.39	2.433 ± 0.090	−0.39	2.273 ± 0.094	−0.39	1.977 ± 0.082	−0.39	1.692 ± 0.076
−0.29	1.905 ± 0.072	−0.29	1.834 ± 0.069	−0.29	1.619 ± 0.062	−0.29	1.500 ± 0.063
−0.20	1.681 ± 0.068	−0.20	1.559 ± 0.064	−0.20	1.475 ± 0.073	−0.20	1.298 ± 0.053
−0.10	1.489 ± 0.063	−0.10	1.441 ± 0.063	−0.10	1.327 ± 0.054	−0.09	1.257 ± 0.057
0.00	1.433 ± 0.062	0.00	1.444 ± 0.060	0.00	1.341 ± 0.060	0.00	1.179 ± 0.061
0.10	1.514 ± 0.061	0.10	1.561 ± 0.064	0.10	1.347 ± 0.058	0.10	1.381 ± 0.071
0.20	1.689 ± 0.075	0.20	1.657 ± 0.064	0.20	1.502 ± 0.072	0.20	1.597 ± 0.066
0.31	1.779 ± 0.070	0.31	1.890 ± 0.078	0.30	1.806 ± 0.081	0.30	1.792 ± 0.070
0.40	2.122 ± 0.083	0.40	2.221 ± 0.084	0.40	2.073 ± 0.079	0.40	2.117 ± 0.077
0.50	2.358 ± 0.078	0.50	2.324 ± 0.077	0.50	2.294 ± 0.077	0.50	2.196 ± 0.076
0.61	2.515 ± 0.084	0.61	2.521 ± 0.084	0.61	2.415 ± 0.085	0.61	2.427 ± 0.090

$\cos(\theta_{\mathrm{cm}})$	$E_\gamma = 1096$ MeV
−0.98	1.534 ± 0.137
−0.90	1.776 ± 0.116
−0.80	1.909 ± 0.069
−0.70	1.889 ± 0.060
−0.60	1.838 ± 0.062
−0.51	1.748 ± 0.083
−0.39	1.687 ± 0.089
−0.29	1.345 ± 0.074
−0.19	1.253 ± 0.068
−0.09	1.078 ± 0.073
0.00	1.318 ± 0.083
0.10	1.275 ± 0.068
0.20	1.486 ± 0.076
0.30	1.797 ± 0.110
0.40	2.082 ± 0.101
0.50	2.253 ± 0.098
0.61	2.310 ± 0.113

Table 6. Differential cross-sections $d\sigma/d\Omega$ (μb/sr) for photon energies 1107 MeV $\leq E_\gamma \leq$ 1418 MeV.

$\cos(\theta_{cm})$	$E_\gamma = 1107$ MeV	$\cos(\theta_{cm})$	$E_\gamma = 1137$ MeV	$\cos(\theta_{cm})$	$E_\gamma = 1167$ MeV	$\cos(\theta_{cm})$	$E_\gamma = 1196$ MeV
−0.95	1.382 ± 0.070	−0.95	1.115 ± 0.054	−0.95	1.141 ± 0.056	−0.95	1.185 ± 0.063
−0.85	1.439 ± 0.062	−0.85	1.178 ± 0.052	−0.85	1.072 ± 0.049	−0.85	1.047 ± 0.049
−0.75	1.571 ± 0.078	−0.75	1.227 ± 0.063	−0.75	1.028 ± 0.054	−0.75	0.987 ± 0.054
−0.65	1.472 ± 0.117	−0.65	1.087 ± 0.084	−0.65	0.873 ± 0.079	−0.65	0.831 ± 0.060
−0.55	1.400 ± 0.103	−0.55	1.112 ± 0.093	−0.55	0.935 ± 0.092	−0.55	0.736 ± 0.072
−0.45	1.276 ± 0.097	−0.45	1.002 ± 0.100	−0.45	0.811 ± 0.071	−0.45	0.686 ± 0.068
−0.35	1.208 ± 0.085	−0.35	0.882 ± 0.066	−0.35	0.777 ± 0.065	−0.35	0.641 ± 0.055
−0.25	1.107 ± 0.082	−0.25	0.868 ± 0.075	−0.25	0.740 ± 0.059	−0.25	0.609 ± 0.051
−0.15	1.041 ± 0.065	−0.15	0.809 ± 0.056	−0.15	0.705 ± 0.065	−0.15	0.677 ± 0.057
−0.05	1.004 ± 0.074	−0.05	0.832 ± 0.058	−0.05	0.794 ± 0.058	−0.05	0.767 ± 0.072
0.05	1.156 ± 0.074	0.05	0.892 ± 0.065	0.05	0.901 ± 0.083	0.05	0.840 ± 0.066
0.15	1.266 ± 0.081	0.15	1.135 ± 0.084	0.15	0.925 ± 0.067	0.15	0.856 ± 0.068
0.25	1.401 ± 0.084	0.25	1.295 ± 0.088	0.25	1.124 ± 0.084	0.25	0.979 ± 0.091
0.35	1.732 ± 0.108	0.35	1.465 ± 0.108	0.35	1.185 ± 0.116	0.35	0.982 ± 0.089
0.45	1.880 ± 0.112	0.45	1.461 ± 0.093	0.45	1.383 ± 0.106	0.45	1.080 ± 0.086
0.55	2.033 ± 0.111	0.55	1.630 ± 0.104	0.55	1.264 ± 0.097	0.55	1.162 ± 0.092
0.65	1.980 ± 0.134	0.65	1.613 ± 0.118	0.65	1.333 ± 0.109	0.65	1.140 ± 0.108
$\cos(\theta_{cm})$	$E_\gamma = 1225$ MeV	$\cos(\theta_{cm})$	$E_\gamma = 1253$ MeV	$\cos(\theta_{cm})$	$E_\gamma = 1282$ MeV	$\cos(\theta_{cm})$	$E_\gamma = 1310$ MeV
−0.95	1.229 ± 0.063	−0.95	1.337 ± 0.071	−0.95	1.353 ± 0.070	−0.95	1.446 ± 0.072
−0.85	1.032 ± 0.051	−0.85	1.169 ± 0.054	−0.85	1.220 ± 0.056	−0.85	1.278 ± 0.064
−0.75	0.968 ± 0.056	−0.75	0.987 ± 0.054	−0.75	1.004 ± 0.056	−0.75	1.038 ± 0.059
−0.65	0.765 ± 0.055	−0.65	0.821 ± 0.060	−0.65	0.797 ± 0.056	−0.65	0.831 ± 0.067
−0.55	0.693 ± 0.061	−0.55	0.700 ± 0.063	−0.55	0.635 ± 0.074	−0.55	0.651 ± 0.056
−0.45	0.598 ± 0.058	−0.45	0.588 ± 0.061	−0.45	0.551 ± 0.062	−0.45	0.633 ± 0.072
−0.35	0.632 ± 0.057	−0.35	0.594 ± 0.061	−0.35	0.548 ± 0.053	−0.35	0.542 ± 0.050
−0.25	0.581 ± 0.056	−0.25	0.574 ± 0.051	−0.25	0.552 ± 0.055	−0.25	0.591 ± 0.051
−0.15	0.613 ± 0.051	−0.15	0.604 ± 0.052	−0.15	0.681 ± 0.063	−0.15	0.738 ± 0.062
−0.05	0.687 ± 0.057	−0.05	0.633 ± 0.054	−0.05	0.700 ± 0.058	−0.05	0.702 ± 0.059
0.05	0.733 ± 0.064	0.05	0.714 ± 0.068	0.05	0.656 ± 0.053	0.05	0.677 ± 0.065
0.15	0.775 ± 0.073	0.15	0.755 ± 0.074	0.15	0.817 ± 0.073	0.15	0.757 ± 0.071
0.25	0.892 ± 0.079	0.25	0.817 ± 0.077	0.25	0.812 ± 0.079	0.25	0.724 ± 0.071
0.35	0.911 ± 0.083	0.35	0.865 ± 0.083	0.35	0.752 ± 0.081	0.35	0.671 ± 0.071
0.45	0.944 ± 0.088	0.45	0.734 ± 0.072	0.45	0.778 ± 0.096	0.45	0.650 ± 0.076
0.55	0.933 ± 0.092	0.55	0.844 ± 0.087	0.55	0.751 ± 0.072	0.55	0.677 ± 0.065
0.65	1.004 ± 0.102	0.65	0.962 ± 0.111	0.65	0.931 ± 0.119	0.65	0.916 ± 0.129
$\cos(\theta_{cm})$	$E_\gamma = 1338$ MeV	$\cos(\theta_{cm})$	$E_\gamma = 1364$ MeV	$\cos(\theta_{cm})$	$E_\gamma = 1392$ MeV	$\cos(\theta_{cm})$	$E_\gamma = 1418$ MeV
−0.95	1.480 ± 0.071	−0.95	1.451 ± 0.068	−0.95	1.513 ± 0.071	−0.95	1.497 ± 0.069
−0.85	1.330 ± 0.058	−0.85	1.361 ± 0.060	−0.85	1.376 ± 0.068	−0.85	1.384 ± 0.057
−0.75	1.109 ± 0.060	−0.75	1.153 ± 0.068	−0.75	1.069 ± 0.055	−0.75	1.073 ± 0.053
−0.65	0.794 ± 0.054	−0.65	0.829 ± 0.063	−0.65	0.794 ± 0.058	−0.65	0.851 ± 0.053
−0.55	0.694 ± 0.060	−0.55	0.663 ± 0.062	−0.55	0.639 ± 0.053	−0.55	0.666 ± 0.053
−0.45	0.617 ± 0.082	−0.45	0.581 ± 0.056	−0.45	0.621 ± 0.061	−0.45	0.625 ± 0.058
−0.35	0.562 ± 0.051	−0.35	0.609 ± 0.058	−0.35	0.606 ± 0.059	−0.35	0.664 ± 0.066
−0.25	0.695 ± 0.065	−0.25	0.625 ± 0.056	−0.25	0.668 ± 0.053	−0.25	0.761 ± 0.058
−0.15	0.721 ± 0.060	−0.15	0.778 ± 0.066	−0.15	0.823 ± 0.071	−0.15	0.797 ± 0.060
−0.05	0.708 ± 0.056	−0.05	0.820 ± 0.066	−0.05	0.853 ± 0.075	−0.05	0.874 ± 0.067
0.05	0.759 ± 0.065	0.05	0.752 ± 0.059	0.05	0.814 ± 0.065	0.05	0.813 ± 0.063
0.15	0.754 ± 0.067	0.15	0.762 ± 0.069	0.15	0.729 ± 0.075	0.15	0.739 ± 0.073
0.25	0.716 ± 0.076	0.25	0.657 ± 0.085	0.25	0.692 ± 0.075	0.25	0.560 ± 0.061
0.35	0.617 ± 0.075	0.35	0.557 ± 0.074	0.35	0.485 ± 0.060	0.35	0.465 ± 0.060
0.45	0.542 ± 0.061	0.45	0.488 ± 0.059	0.45	0.408 ± 0.051	0.45	0.362 ± 0.056
0.55	0.612 ± 0.061	0.55	0.560 ± 0.056	0.55	0.566 ± 0.060	0.55	0.466 ± 0.047
0.65	0.980 ± 0.174	0.65	0.776 ± 0.118	0.65	0.805 ± 0.140	0.65	0.899 ± 0.199

Table 7. Differential cross-sections $d\sigma/d\Omega$ (μb/sr) for photon energies 1444 MeV $\leq E_\gamma \leq$ 1541 MeV.

$\cos(\theta_{cm})$	$E_\gamma = 1444$ MeV	$\cos(\theta_{cm})$	$E_\gamma = 1470$ MeV	$\cos(\theta_{cm})$	$E_\gamma = 1496$ MeV	$\cos(\theta_{cm})$	$E_\gamma = 1521$ MeV
−0.95	1.331 ± 0.062	−0.95	1.280 ± 0.072	−0.95	1.104 ± 0.062	−0.95	0.999 ± 0.058
−0.85	1.321 ± 0.057	−0.85	1.153 ± 0.056	−0.85	1.149 ± 0.056	−0.85	1.035 ± 0.051
−0.75	1.016 ± 0.050	−0.75	0.965 ± 0.055	−0.75	0.879 ± 0.050	−0.75	0.833 ± 0.048
−0.65	0.772 ± 0.047	−0.65	0.774 ± 0.054	−0.65	0.690 ± 0.049	−0.65	0.644 ± 0.045
−0.55	0.598 ± 0.048	−0.55	0.629 ± 0.054	−0.55	0.554 ± 0.048	−0.55	0.541 ± 0.047
−0.45	0.567 ± 0.051	−0.45	0.528 ± 0.053	−0.45	0.533 ± 0.054	−0.45	0.532 ± 0.053
−0.35	0.606 ± 0.052	−0.35	0.549 ± 0.055	−0.35	0.657 ± 0.068	−0.35	0.689 ± 0.070
−0.25	0.730 ± 0.057	−0.25	0.865 ± 0.085	−0.25	0.734 ± 0.069	−0.25	0.825 ± 0.079
−0.15	0.925 ± 0.075	−0.15	0.978 ± 0.093	−0.15	0.891 ± 0.083	−0.15	0.852 ± 0.079
−0.05	0.826 ± 0.080	−0.05	0.897 ± 0.091	−0.05	0.904 ± 0.087	−0.05	0.860 ± 0.087
0.05	0.785 ± 0.062	0.05	0.800 ± 0.081	0.05	0.797 ± 0.081	0.05	0.917 ± 0.093
0.15	0.739 ± 0.074	0.15	0.642 ± 0.077	0.15	0.766 ± 0.096	0.15	0.876 ± 0.118
0.25	0.530 ± 0.074	0.25	0.612 ± 0.086	0.25	0.596 ± 0.089	0.25	0.608 ± 0.091
0.35	0.387 ± 0.049	0.35	0.400 ± 0.068	0.35	0.370 ± 0.066	0.35	0.259 ± 0.048
0.45	0.337 ± 0.051	0.45	0.302 ± 0.053	0.45	0.400 ± 0.082	0.45	0.217 ± 0.039
0.55	0.461 ± 0.048	0.55	0.429 ± 0.056	0.55	0.375 ± 0.049	0.55	0.468 ± 0.064
0.65	0.930 ± 0.243						

$\cos(\theta_{cm})$	$E_\gamma = 1541$ MeV
−0.95	0.963 ± 0.071
−0.85	0.939 ± 0.056
−0.75	0.808 ± 0.057
−0.65	0.559 ± 0.050
−0.55	0.533 ± 0.058
−0.45	0.466 ± 0.058
−0.35	0.613 ± 0.084
−0.25	0.757 ± 0.091
−0.15	0.787 ± 0.098
−0.05	0.909 ± 0.113
0.05	0.770 ± 0.100
0.15	0.708 ± 0.131
0.25	0.378 ± 0.073
0.35	0.288 ± 0.079
0.45	0.230 ± 0.060
0.55	0.332 ± 0.061

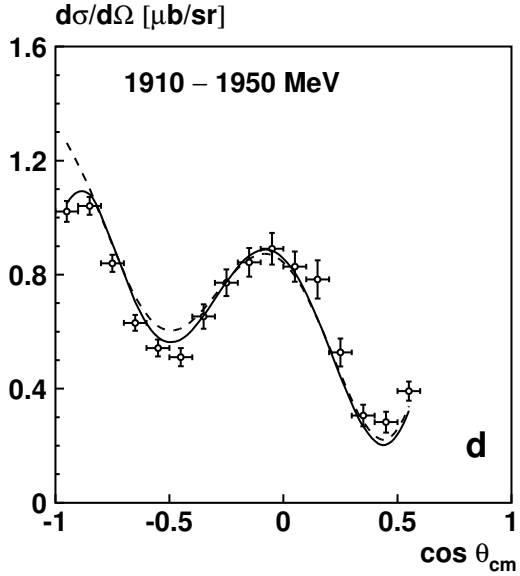

Fig. 18. Differential cross-sections for W = 1910–1950 MeV (E_γ = 1480–1560 MeV). The Bonn PWA fit with the new resonance $N(2070)D_{15}$ is shown as solid line; the dashed line shows a fit when the $5/2^-$ resonance is replaced by a $7/2^-$ state.

Our results on both observables have brought essential constraints to the fit. On the one hand, Σ has allowed to restrict the number of contributing resonances. On the other hand, $d\sigma/d\Omega$ helped to determine the spin of $N(2070)D_{15}$, one of the hypothetical new resonances. As shown in fig. 18, a spin-parity of $5/2^-$ for the resonance is favored by the backward angular distribution measured at $W = 1930$ MeV ($E_\gamma = 1520$ MeV).

Thanks to the recent improvements in the three models, an excellent overall agreement is now achieved despite the variety of observed structures *versus* energy, underlining the presence of a large number of resonant contributions. It should be noted that significant differences remain in the extracted resonance parameters, even for the most prominent ones. However, the procedures of extraction largely differ from one model to another, as well as the used database.

5 Summary

In this paper, we have presented new results on π^0 photoproduction on the proton from 550 to 1500 MeV. Precise measurements for both differential cross-sections and

beam asymmetries have been obtained. These results complement the pion photoproduction database and extend the beam asymmetry measurements up to 1500 MeV. We have compared our results with three models, which are able to fit the whole set of data and bring interesting new information. Like for our previous results on $\pi^+ n$ and ηp, the $\pi^0 p$ beam asymmetry turned out to be a valuable information for the models.

We are grateful to A.V. Anisovich, S. Kamalov, E. Klempt and L. Tiator for fruitful discussions and communication of their analyses prior to publication. It is a pleasure to thank the ESRF as a host institution and its technical staff for the smooth operation of the beam. Technical assistance of all participating institutions is greatly acknowledged.

References

1. J.P Bocquet, V. Kuznetsov, D. Rebreyend (Editors), *Proceedings of the Workshop on the Physics of Excited Nucleons, NSTAR2004* (World Scientific, 2004).
2. *Review of Particle Physics 2004*, Phys. Lett. B **592**, 1 (2004).
3. R. Beck *et al.*, Phys. Rev. C **61**, 035204 (2000).
4. G. Blanpied *et al.*, Phys. Rev. C **64**, 025203 (2001).
5. J. Ajaka *et al.*, Phys. Rev. Lett. **81**, 1797 (1998).
6. J. Ajaka *et al.*, Phys. Lett. B **475**, 372 (2000).
7. O. Bartalini *et al.*, Phys. Lett. B **544**, 113 (2002).
8. Y. Assafiri *et al.*, Phys. Rev. Lett. **90**, 222001 (2003).
9. Z. Li, B. Saghai, Nucl. Phys. A **644**, 345 (1998).
10. N. Mukhopahyay, N. Mathur, Phys. Lett. B **444**, 7 (1998).
11. L. Tiator *et al.*, Phys. Rev. C **60**, 035210 (1999).
12. R. Workman *et al.*, Phys. Rev. C **62**, 048201 (2000).
13. V. Bellini *et al.*, Nucl. Instrum. Methods A **386**, 254 (1997).
14. F. Renard, Thesis, Université J. Fourier (Grenoble) 1999, unpublished.
15. C. Fry, MSci research project at Imperial College, LPSC internal report 2002, unpublished.
16. F.R. Arutyunian *et al.*, Teor. Fiz. **45**, 312 (1963).
17. L. Nicoletti, Thesis, Université J. Fourier (Grenoble) 2002, unpublished.
18. P. Levi Sandri *et al.*, Nucl. Instrum. Methods A **370**, 396 (1996).
19. M. Castoldi *et al.*, Nucl. Instrum. Methods A **403**, 22 (1998).
20. F. Ghio *et al.*, Nucl. Instrum. Methods A **404**, 71 (1998).
21. V. Kouznetsov *et al.*, Nucl. Instrum. Methods A **487**, 396 (2002).
22. D. Barancourt *et al.*, Nucl. Instrum. Methods A **388**, 226 (1997).
23. L. Mazzaschi *et al.*, Nucl. Instrum. Methods A **436**, 441 (1994).
24. F. Renard *et al.*, Phys. Lett. B **528**, 215 (2002).
25. The full data set is available at the website `http://lpsc.in2p3.fr/GRAAL1`.
26. F.V. Adamian *et al.*, Phys. Rev. C **63**, 054606 (2001).
27. O. Bartholomy *et al.*, Phys. Rev. Lett. **94**, 012003 (2005).
28. R.A. Arndt *et al.*, Phys. Rev. C **66**, 055213 (2002).
29. SAID-FA04, website `http://gwdac.phys.gwu.edu`.
30. L. Tiator *et al.*, Eur. Phys. J. A **19**, S01, 55 (2004).
31. S.S. Kamalov, L. Tiator, MAID2005, private communication.
32. L. Tiator *et al.*, *Proceedings of the Workshop on the Physics of Excited Nucleons, NSTAR2005*, to be published by World Scientific.
33. A.V. Anisovich *et al.*, Phys. Rev. C **68**, 045202 (2003).
34. A.V. Anisovich *et al.*, Eur. Phys. J. A **25**, 427 (2005).